# Local Current Density Calculations for Molecular Films from *Ab Initio*

Michael Walz,*[,†,‡] Alexei Bagrets,[†] and Ferdinand Evers[§]

[†]Institute of Nanotechnology, Karlsruhe Institute of Technology, Campus North, D-76131 Karlsruhe, Germany
[‡]Institut für Theorie der Kondensierten Materie, Karlsruhe Institute of Technology, Campus South, D-76131 Karlsruhe, Germany
[§]Institute for Theoretical Physics, University of Regensburg, D-93040 Regensburg, Germany

ABSTRACT: We present a formalism relying on density functional theory for the calculation of the spatially continuous electron current density $\mathbf{j}(\mathbf{r})$ and induced magnetic fields $\mathbf{B}(\mathbf{r})$ in molecular films in dc transport. The proposed method treats electron transport in graphene ribbons containing on the of order 10^3 atoms. The employed computational techniques scale efficiently when using several thousand CPUs. An application to transport through hydrogenated graphene will be presented. As we will show, the adatoms have an impact on the transmission function not only because they introduce additional states but also because their presence modifies the geometry of the carbon host lattice (lattice relaxation).
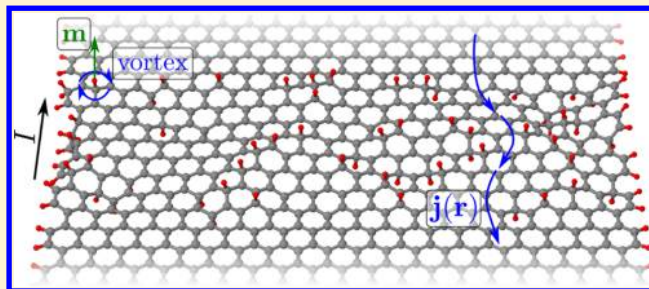
1. INTRODUCTION

In transport experiments through molecular films like graphene,[1−3] e.g., hydrogenated armchair graphene nanoribbons (Figure 1), the question of how currents flow through the
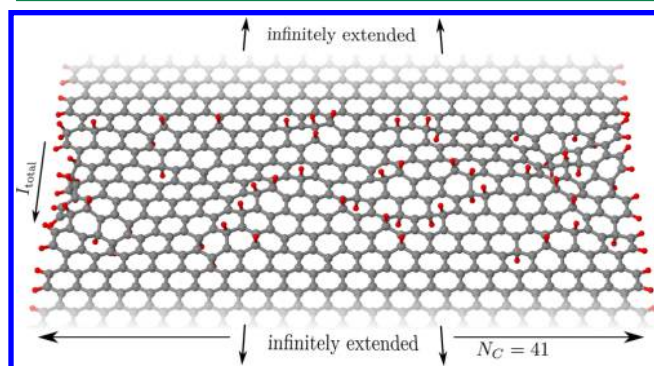
Figure 1. Atomic structure of a wide hydrogen-terminated armchair graphene nanoribbon (41×8) with $N_C = 41$ carbon atoms in the transverse direction (AGNR41). The nanoribbon has been functionalized with an additional 20% of hydrogen atoms (66 additional hydrogen atoms). Appying a bias voltage between the (infinitely extended) upper and lower leads results in a current flow across the device.

device is fundamental. One often focuses on a few global observables, such as current−voltage ($I−V$) curves, which describe the experimental setup as a whole. An established concept to deal with such $I−V$ curves is the Landauer−Büttiker formalism, which allows the total current to be related to the calculation of a few transmission coefficients.

Reducing the complexity in such a way also eliminates fundamental physics, in this case, the spatial dependency of the

electron current density $\mathbf{j}(\mathbf{r})$, which describes the pathway through the structure. The current patterns are inhomogeneous, even in clean molecular films, due to the presence of confining edges.[4] When including scatterers, ring patterns emerge (current vortices) that do not contribute to the transport current and therefore are not seen (directly) in the $I−V$ curve. Such vortices induce local magnetic fields $\mathbf{B}(\mathbf{r})$ with spatial fluctuations on the atomic scale.[5]

In this article, we explain our calculations of the local current densities $\mathbf{j}(\mathbf{r})$ and the related induced local magnetic fields $\mathbf{B}(\mathbf{r})$. To this end, we apply the nonequilibrium Green's function (NEGF) formalism to (independent) Kohn−Sham particles. The procedure is general and could also be implemented in other NEGF codes[6−13] that rely on density functional theory (DFT). Existing codes focus on global quantities like the transmission coefficients or the current−voltage characteristics. Examples include DFT-based tight-binding codes, like gDFTB[6] implemented on top of DFTB+,[14] as well as full DFT codes, like TRANSIESTA,[7] SMEAGOL[8,9] (both based on the DFT code SIESTA[15]), or WANT[10] (based on QUANTUM ESPRESSO[16]).

Microscopic transport simulations of graphene materials are often based on tight-binding models with a single spatial orbital per atom.[17−25] They outperform *ab initio* based methods in terms of computational effort. On the other hand, on a microscopic level only bond currents are available with them, i.e., current contributions flowing from one lattice site to another.[17−22] Calculations of $\mathbf{j}(\mathbf{r})$ or of the induced magnetic field $\mathbf{B}(\mathbf{r})$ on atomic length scales can be done only if the spatial structure of wave functions is reinstalled, which usually is quite cumbersome.[26]

For this purpose, full fledged *ab initio* simulations with several basis functions per atoms are useful. Here, we explain an implementation of the calculation of the local current densities and induced magnetic fields within our transport framework AITRANSS,[27−29] which is already interfaced with the *ab initio* packages FHI-AIMS[30] and TURBOMOLE.[31] The basic idea is to construct the Kohn−Sham (KS) scattering states $\psi(\mathbf{r})$ from the underlying DFT simulation and employ the Landauer−Büttiker approach to independent particles to compute the KS electron current density. The latter can be formally viewed as

$$\mathbf{j}(\mathbf{r}) = \frac{\hbar}{2im} \lim_{\mathbf{r}' \to \mathbf{r}} (\nabla_{\mathbf{r}} - \nabla_{\mathbf{r}'}) \psi^*(\mathbf{r}')\, \psi(\mathbf{r}) \tag{1}$$

per KS scattering state.

To keep the computational effort tractable, we employ the massively parallelized *ab initio* package FHI-AIMS, whose scalability has already been demonstrated up to several thousand CPUs.[30,32−34] To preserve this scalability, shared-memory (via OpenMP) and distributed-memory (via MPI) parallelization approaches are implemented in the transport module. It is readily adapted to other electronic structure codes that deliverer all (occupied and virtual) eigenstates in terms of local basis functions. To illustrate its flexibility, we will also present applications based on the TURBOMOLE package.

Our methodology has already been applied in separate publications.[4,5,35] Here, we provide details of the implementation, tests, and a further application that reveals the effect of lattice relaxation on the transmission function. In Section 2, we summarize the transport formalism used, which is based on the NEGF technique. This includes the construction of self-energies to model the semi-infinite leads. In Section 3, we extract the KS-Hamiltonian of a finite system from the DFT calculation. The calculation and convergence tests for local current densities and the application to lattice relaxations are presented in Section 4, whereas the induced local magnetic fields are discussed in Section 5. We close with an investigation of the computational performance (Section 6).

2. METHOD

2.1. *Ab Initio* Transport Calculation in Landauer−Büttiker Picture.
Electron transport calculations are performed with the module AITRANSS.[27−29] It reconstructs the KS-Hamiltonian $\mathbf{H}^{KS}$ from a local orbital (ground state) DFT calculation (for details, see Section 3) and then applies the Landauer−Büttiker approach in a formulation with NEGFs.

It should be noted that the KS-based Landauer formalism has been established to reproduce the exact (physical) conductance only in two model situations: for noninteracting particles and in the presence of strong correlations, namely, in the framework of the single impurity Anderson model (SIAM).[36−40] Our implementation aims at intermediate situations, with interaction effects that can be modeled qualitatively by effective local potentials and corresponding excitations with a single-particle nature. With this caveat, we expect the general qualitative features of our simulation results to be representative of the real physical system, in particular, the tendencies to form ring currents or streamline patterns. although the actual flow pattern for a given atomic arrangement of device might somewhat deviate from our simulations.

2.1.1. *Standard Transmission Calculation.*
To be more specific and to recall the basic definitions, we consider an example, a thin armchair graphene nanoribbon (AGNR5), as shown in Figure 2. We partition it into a central region
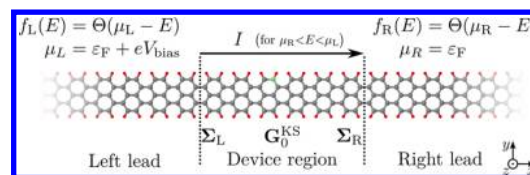
Figure 2. Armchair graphene nanoribbon partitioned into a left lead, right lead, and central region containing one nitrogen impurity (green).

(device), a left lead, and a right lead. We extract the KS Green's function $\mathbf{G}_0^{KS}(E)$

$$\mathbf{G}_0^{KS}(E) = (E\mathbf{1} - \mathbf{H}^{KS} + i0)^{-1} \tag{2}$$

for the uncoupled device from the DFT calculations. To model the infinite extension of the system in the (current flow) x-direction, we compute the self-energies $\mathbf{\Sigma}_{L/R}$ using absorbing boundary conditions[41] as specified in Section 2.2. The resulting Green's function

$$\mathbf{G}(E)^{-1} = \mathbf{G}_0^{KS}(E)^{-1} - \mathbf{\Sigma}_L(E) - \mathbf{\Sigma}_R(E) \tag{3}$$

describes the propagation of KS particles in the device in the presence of leads and is used to calculate the transmission $\mathcal{T}(E)$ through the system

$$\mathcal{T}(E) = \mathrm{Tr}\{\mathbf{\Gamma}_L \mathbf{G} \mathbf{\Gamma}_R \mathbf{G}^{\dagger}\} \tag{4}$$

Here, $\mathbf{\Gamma}_{L/R}$ denote the anti-Hermitian parts of the self-energies, i.e., $\mathbf{\Gamma}_{L/R} = i(\mathbf{\Sigma}_{L/R} - \mathbf{\Sigma}_{L/R}^{\dagger})$. They account for the level broadenings in the device region due to the coupling to the leads.

When a bias voltage is applied between the leads, $(-e)V_{bias} = \mu_R - \mu_L$, the total electric current (per spin) is given by

$$I_e = \frac{-e}{h} \int_{-\infty}^{+\infty} dE\, \mathcal{T}(E)(f_L(E) - f_R(E)) \tag{5}$$

which depends on the occupation numbers $f_{L/R}(E)$ of the left- and right-traveling scattering states. For low temperatures, the occupation numbers can be modeled by step functions [$f_L = \Theta(\mu_L - E)$, $f_R = \Theta(\mu_R - E)$], and the total electric current simplifies to

$$I_e = \frac{-e}{h} \int_{\mu_R}^{\mu_L} dE\, \mathcal{T}(E) \tag{6}$$

2.1.2. *Local Observables: Current Density and Induced B-Field.*
The Green's function $\mathbf{G}(E)$ also allows the non-equilibrium Keldysh Green's function $\mathbf{G}^<(E)$ to be calculated

$$\mathbf{G}^< = i\mathbf{G}[f_L \mathbf{\Gamma}_L + f_R \mathbf{\Gamma}_R]\mathbf{G}^{\dagger} \tag{7}$$

At $T = 0$ and at energies $\mu_R \leq E \leq \mu_L$, i.e., inside the voltage window, one has $f_L = 1$ and $f_R = 0$, so $\mathbf{G}^<$ reduces to

$$\mathbf{G}^<(E) = i\mathbf{G}(E)\, \mathbf{\Gamma}_L(E)\, \mathbf{G}^{\dagger}(E) \tag{8}$$

The Keldysh Green's function is transformed to a real-space representation using the orthonormalized basis functions $\tilde{\varphi}_i(\mathbf{r})$ based on the underlying DFT calculation

$$\mathbf{G}^<(\mathbf{r},\mathbf{r}',E) = \sum_{ij} \tilde{\varphi}_i(\mathbf{r})\, \mathbf{G}_{ij}^<(E)\, \tilde{\varphi}_j^*(\mathbf{r}') \tag{9}$$

Using this decomposition, the current density (per spin and energy) is expressed as

$$\mathbf{j}(\mathbf{r},E) = \frac{1}{2\pi}\frac{\hbar}{2m}\lim_{\mathbf{r}'\to\mathbf{r}}(\nabla_{\mathbf{r}'} - \nabla_{\mathbf{r}})\,\mathbf{G}^<(\mathbf{r},\mathbf{r}',E) \tag{10}$$

see Section 4 for details. The factor 2π reflects the Fourier transformation. When applying a finite bias voltage V_{bias} between the left and right leads, current contributions within the bias window are integrated, i.e.

$$\mathbf{j}(\mathbf{r}) = \int_{\mu_R}^{\mu_L} dE\,\mathbf{j}(\mathbf{r},E) \tag{11}$$

The current response to the bias voltage (at zero bias) is given by

$$\left.\frac{d\mathbf{j}(\mathbf{r})}{d(-eV_{bias})}\right|_{V_{bias}=0} = \mathbf{j}(\mathbf{r},\varepsilon_F) \tag{12}$$

The Fermi energy ε_F can be varied experimentally, e.g., by applying a back-gate voltage V_{gate}.

Furthermore, the electric current density $\mathbf{j}_e = -e\mathbf{j}$ induces a magnetic field $\mathbf{B}$ and a magnetization $\mathbf{m}$, which is calculated via the Biot–Savart law as

$$\mathbf{B}(\mathbf{r}) = \frac{\mu_0}{4\pi}\int\frac{\mathbf{j}_e(\mathbf{r}')\times(\mathbf{r}-\mathbf{r}')}{|\mathbf{r}-\mathbf{r}'|^3}d^3\mathbf{r}' \tag{13}$$

$$\mathbf{m} = \frac{1}{2}\int\mathbf{r}\times\mathbf{j}_e(\mathbf{r})\,d^3\mathbf{r} \tag{14}$$

2.1.2.1. Remark on Finite Basis Sets. The current density as written in eq 10 satisfies a continuity equation in the basis set limit: $\nabla\cdot\mathbf{j}(\mathbf{r}) = 0$. For finite basis sets, this equation is violated. The magnitude $|\nabla\cdot\mathbf{j}|$ decreases with increasing basis set size. At the end of all calculations, one has to ensure that the basis set was large enough so that $\nabla\cdot\mathbf{j} \approx 0$.

2.2. Modeling the Infinite System: Construction of the Self-Energy.
The NEGF includes the left and right electrodes (reservoirs) via the corresponding self-energies. They are readily calculated if the reservoir is quasi-one-dimensional, i.e., a "long wire", if two conditions hold true: first, that single particle theory can be applied; second, that the hopping along the wire is short-range. In that case, the lead can be represented by a Hamiltonian that exhibits the following tridiagonal block structure

$$\mathbf{H}^{lead} = \begin{pmatrix} \mathbf{H}^{block}_{[0]} & \mathbf{V} & & 0 \\ \mathbf{V}^\dagger & \mathbf{H}^{block}_{[1]} & \ddots & \\ & \ddots & \ddots & \mathbf{V} \\ 0 & & \mathbf{V}^\dagger & \mathbf{H}^{block}_{[M-1]} \end{pmatrix} \tag{15}$$

Each one of the blocks may be thought of as a "slice" of the original wire; eq 15, therefore, corresponds to a wire consisting of M slices. Every slice is characterized by its own block Hamiltonian, $\mathbf{H}^{block}_{[j]}$. For simplicity, we assume that each slice is described by the same block matrix, $\mathbf{H}^{block}_{[n]} = \mathbf{H}^{block}$, and that each slice connects to the other slices via a block matrix $\mathbf{V}$ that is the same for every pair of neighboring slices (and zero otherwise). It is easy to see that, due to the tridiagonal block structure, self-energy is readily calculated in a recursive fashion.[42] We have

$$\mathbf{\Sigma}^m(E) = \mathbf{V}^\dagger\mathbf{G}^{m-1}(E)\mathbf{V}, \qquad \mathbf{\Sigma}^0(E) = 0 \tag{16}$$

with

$$\mathbf{G}^m(E) = [(E + i\eta_{dec})\mathbf{1} - \mathbf{H}^{block}_{[m]} - \mathbf{\Sigma}^m(E)]^{-1} \tag{17}$$

The number of blocks M that it takes to converge the self-energies depends on the imaginary shift η_{dec}; typically, we have $M = 50$–400. (Therefore, it would be numerically too expensive to calculate the lead's Green's function $\mathbf{G}^{lead} = [(E + i\eta_{dec})\mathbf{1} - \mathbf{H}^{lead}]^{-1}$ by full matrix inversion.) This set of recursion equations is often referred to as the block decimation technique. On a mathematical level, it is effectively a Gaussian elimination scheme.

In the final step, we make use of the fact that the full Hamiltonian, including the left and right leads together with the device, again has a block structure

$$\mathbf{H} = \begin{pmatrix} \mathbf{H}^{lead} & \mathbf{V}_L & 0 \\ \mathbf{V}_L^\dagger & \mathbf{H}^{device} & \mathbf{V}_R^\dagger \\ 0 & \mathbf{V}_R & \mathbf{H}^{lead} \end{pmatrix} \tag{18}$$

For simplicity, we assume here that the left and right leads are twins. Then, we evaluate self-energies for the left and right leads along the same line as before

$$\mathbf{\Sigma}_\alpha^M = \mathbf{V}_\alpha^\dagger\mathbf{G}_\alpha^{M-1}\mathbf{V}_\alpha, \qquad \alpha = R, L \tag{19}$$

The Green's function for an arbitrary device $\mathbf{H}^{device}$ in the presence of the leads is readily found via matrix inversion

$$\mathbf{G}(E) = [E\mathbf{1} - \mathbf{H}^{device} - \mathbf{\Sigma}_L^M(E) - \mathbf{\Sigma}_R^M(E)]^{-1} \tag{20}$$

The Green's function $\mathbf{G}(E)$ thus found is used to compute the transmission coefficient (eq 4) and the electron current density (eq 10; see Section 4 for details).

2.2.1. Self-Energy Recycling. The construction of the self-energies does not make explicit reference to the device Hamiltonian $\mathbf{H}^{device}$. Therefore, as long as different devices share the same coupling matrices $\mathbf{V}_{L/R}$, they also share the same self-energies. Hence, it can be computationally advantageous to store them on the hard disk to prepare for recycling. Recycling can be used, e.g., for treating AGNRs with different impurity configurations.

2.2.2. Absorbing Boundary Conditions. The decimation technique (DT) gives a numerically exact result for the self-energy. It is efficient with quasi-one-dimensional wires and short-range hopping.

In its standard implementation, DT works with a (spatially) constant damping rate η_{dec}. In order to generate an effectively smooth lead density of states near ε_F, its magnitude should somewhat exceed the level spacing, $\eta_{dec} \gtrsim \Delta(M)$, that decreases with the wire length $\Delta(M) \sim v_F 2\pi\hbar/(Ml)$, where v_F denotes the Fermi velocity and l is the width of each slice.

For realistic modeling, the absorption should occur in the leads, i.e., sufficiently far away from the device. Therefore, a second requirement on η_{dec} is that it should be negligible near the contact to the device. Ideally, η_{dec} vanishes in the device region. Now, if the damping is taken to be spatially constant, then η_{dec} will be small everywhere, so M must be (very) large to satisfy the inequality. Indeed, it turns out that DT is sufficient enough so that, in many cases, the system's size limit can be reached.

Nevertheless, a standard DT (with spatially constant η_{dec}) becomes computationally expensive, e.g., because the coupling matrices $\mathbf{V}$ are large. Therefore, in this work, we combine DT with a spatially varying damping rate

$$\eta(\mathbf{r}) = \eta_0 e^{-\kappa(L-d)}, \qquad \hat{\eta}_{ABC} = \eta(\mathbf{r})\,\delta(\mathbf{r} - \hat{\mathbf{r}}) \qquad (21)$$

where κ is the damping coefficient and d denotes the distance between the device region and the absorption point $\mathbf{r}$ inside the reservoir. L is total length of each lead. The leakage rate (or damping rate) $\eta(\mathbf{r})$ describes how electrons are adsorbed into the leads. We include the spatially varying damping in the DT by replacing η_{dec} with $\hat{\eta}_{ABC}$ in eq 17.

In our previous work, we have already used such a spatially varying damping rate (without DT) to include the reservoirs using model self-energies $\hat{\mathbf{\Sigma}}_{ABC} = -i\hat{\eta}_{ABC}$ that realize Schrödinger-type dynamics with absorbing boundary conditions (ABC).[41] This approach can already be efficient on its own (without DT) when working with Au electrodes of pyramidal shape (provided that enough Au atoms can be kept as a part of the device region in the DFT reference calculation).[27−29] For Au electrodes, it turns out to be difficult to reach the system's size limit with homogeneous damping, while whereas is no problem when the damping is exponentially increased as the distance to the device region increases.

2.2.3. Remark. To resolve the Dirac delta function of eq 21 within the DFT framework, we take advantage of the local basis set: the orthonormal basis functions $|\tilde{\varphi}_i\rangle$ are centered at atoms sitting at position $\mathbf{r}_i$, and we approximate $\langle\tilde{\varphi}_j|\hat{\mathbf{r}}|\tilde{\varphi}_i\rangle \approx \mathbf{r}_i\delta_{ij}$, i.e., $\langle\tilde{\varphi}_j|\hat{\eta}_{ABC}|\tilde{\varphi}_i\rangle = \eta(\mathbf{r}_i)\delta_{ij}$ becomes a diagonal matrix. As default parametrization for the leakage rate, we use the values $\eta_0 = 1$ Ha ≈ 27.2 eV and $\kappa = 16/L$, where L is total length of each lead; see Section 3.3 for validations that this parametrization, indeed, reproduces the correct transport behavior.

2.2.4. Pictorial Illustration. Figure 3 shows an illustration of building the leads, applying the ABC via the damping rates $\eta_{L/R}$, and connecting the leads to the device.
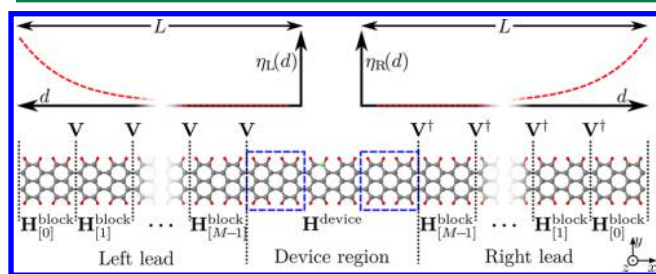
Figure 3. Bottom: Schematic assembly of the total system for transport through AGNR5 with one nitrogen substituent. It consists of left and right leads and a device region. For each lead, M equal building blocks $\mathbf{H}^{block}$ are connected using the coupling matrix $\mathbf{V}$. The device region already contains the beginning of each lead, represented by two contact regions (dashed blue box). Top: Schematic spatial dependence of the leakage rates $\eta(d)$ in the left and right leads as used for absorbing boundary conditions. Near and within the contact region, the leakage rate is exponentially small (nearly zero).

3. KOHN−SHAM HAMILTONIAN

3.1. Reconstruction of the Kohn−Sham Hamiltonian.
So far, the description of the method has been general: the block matrices $\mathbf{H}^{block}$ and $\mathbf{V}$ have not yet been specified. Several effective single-particle descriptions of molecular films (like those shown in Figure 1) are compatible with our methodology, e.g., nearest-neighbor tight-binding models, Hartree−Fock, and DFT. Hartree−Fock (as well as hybrid functionals) are, as in most DFT codes, also available in FHI-AIMS[43] and TURBOMOLE.[31] This allows for comparisons to be easily made, at

least for small systems. We here base the atomistic description on DFT as implemented in the FHI-AIMS and TURBOMOLE packages.[44]

With DFT, a minor complication arises because the matrices $\mathbf{H}^{block}$, $\mathbf{V}$, and $\mathbf{H}^{device}$ refer to the electronic structure of a subsystem embedded in the infinite bulk. For systems with translational invariance, such as clean wires, the block matrices can be extracted from DFT calculations employing plane waves and periodic boundary conditions. In this way, $\mathbf{H}^{block}$ and $\mathbf{V}$ can be found.

In contrast, the device block $\mathbf{H}^{device}$ is not periodic, so a different procedure should be applied here. We extract it from a DFT calculation performed for a finite size block using local basis functions $|\varphi_i\rangle$. A schematic representation of the partitioning is depicted in Figure 4 (left). In addition to the
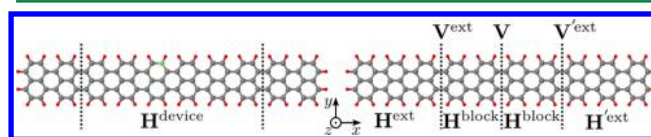
Figure 4. Actual geometry in a DFT calculation of an impurity and a lead system showing the cutting procedure. The armchair graphene nanoribbons (carbon, gray) are terminated with hydrogen (red). The left system contains one nitrogen (green) as an impurity in the central device region.

inner device, we also include a part of the leads in the device block $\mathbf{H}^{device}$ (extended device block), i.e.

$$\mathbf{H}^{device} = \begin{pmatrix} \mathbf{H}^{block} & \cdots & \cdots \\ \cdots & \cdots & \cdots \\ \cdots & \cdots & \mathbf{H}^{block} \end{pmatrix} \qquad (22)$$

In this way, the hybridization matrices, $\mathbf{V}_{L/R}$, which couple the surface of the extended device region to the electrodes, contain the same matrix elements as $\mathbf{V}$.

Due to our choice of a local basis set, the Kohn−Sham (KS) Hamiltonian of the whole system, which contains the extended device, exhibits a block structure. The inner part resembles $\mathbf{H}^{device}$. The extensions have to be chosen to be long enough to ensure the convergence of $\mathbf{H}^{device}$. On a technical level, the procedure is as follows. The KS orbitals $|\psi_i^{mo}\rangle$ are represented by expansion coefficients $\tilde{c}_{ji}$ with respect to the orthogonal basis set $|\tilde{\varphi}_j\rangle$, i.e., $|\psi_i^{mo}\rangle = \sum_j |\tilde{\varphi}_j\rangle\tilde{c}_{ji}$. The orthogonal basis set $|\tilde{\varphi}_j\rangle$ is constructed from the nonorthogonal basis set $|\varphi_j\rangle$ of the underlying DFT calculation using Löwdin orthogonalization (for details, see Appendix A.1).

The device region is associated with the subset of all basis functions $|\tilde{\varphi}_i\rangle$ that are localized on the atoms belonging to the device region. The device block Hamiltonian $\mathbf{H}^{device}$ is given by the matrix elements of the KS-Hamiltonian

$$\hat{\mathcal{H}}_0^{KS} = \sum_n |\psi_n^{mo}\rangle\varepsilon_n^{mo}\langle\psi_n^{mo}| = \sum_{ij} |\tilde{\varphi}_i\rangle\mathbf{H}_{0,ij}^{KS}\langle\tilde{\varphi}_j| \qquad (23)$$

with $\mathbf{H}_{0,ij}^{KS} = \sum_n \tilde{c}_{in}\varepsilon_n^{mo}[\tilde{c}^T]_{nj}$ restricted to the basis functions in the device subset.

By following the same line of ideas, one can also extract the block Hamiltonians for the lead slices, $\mathbf{H}^{block}$ and $\mathbf{V}$, so that there is actually no need to employ a different set of computations with periodic boundary conditions. Specifically, one considers a piece of a homogeneous wire (Figure 4, right) with left and right center slices and extensions to both sides.

The corresponding KS-Hamiltonian will again represent this situation in its block structure when expressed in the localized basis set $|\tilde{\varphi}_i\rangle$:

$$\mathbf{H}^{KS} = \begin{pmatrix} \mathbf{H}^{ext} & \mathbf{V}^{ext} & 0 & 0 \\ \mathbf{V}^{ext\dagger} & \mathbf{H}^{block} & \mathbf{V} & 0 \\ 0 & \mathbf{V}^{\dagger} & \mathbf{H}^{block} & \mathbf{V}'^{ext} \\ 0 & 0 & \mathbf{V}'^{ext\dagger} & \mathbf{H}'^{ext} \end{pmatrix} \quad (24)$$

Once again, the blocks $\mathbf{V}$ and $\mathbf{H}^{block}$ of interest to us are given by the matrix elements of $\mathbf{H}^{KS}$ that are associated with the corresponding left and right subblocks (slices). Again, care has to be taken with the size of the extensions in order to ensure convergence of the center subblocks.

3.1.1. Remark. Ideally, both matrix blocks $\mathbf{H}^{block}$ in eq 24 are identical. In practice, they slightly deviate from each other for finite sized extensions. These deviations are usually small and not important for the transport phenomena; we minimize them by taking the arithmetic average of both matrix blocks (per element with respect to the orthogonal basis set $|\tilde{\varphi}_i\rangle$).

3.2. Convergence Tests for the Kohn–Sham Hamiltonian. We present convergence tests that illustrate how the KS blocks $\mathbf{H}^{block}$ and $\mathbf{V}$ converge with increasing length of the extension, i.e., with a growing distance between the center slices and the (left/right) system's boundaries. To this end, we performed a single DFT run for a long piece of lead electrode. The wire can be cut into slices, and for each slice, the diagonal block $\mathbf{H}^{block}_{[n]}$ (together with the coupling $\mathbf{V}_{[n]}$ to the neighboring blocks) can be extracted. The index n is a measure of the distance from the respective slice to the boundary. Slices sufficiently far away from the boundary ($n \to \infty$) exhibit the same block elements.

As a specific example to illustrate the convergence behavior, we examine pristine AGNR5 in a (spin-unpolarized) DFT calculation.[45] For $n = 0, ..., 9$, we construct several block Hamiltonians $\mathbf{H}^{block}_{[n]}$ for slices that are n carbon rings away from the boundaries (Figure 5). To quantify the deviation $\Delta \mathbf{H}$
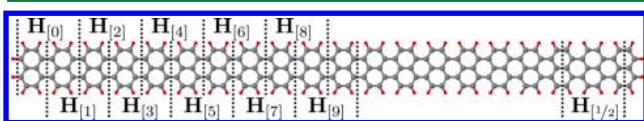
Figure 5. Schematic extraction of the (pairwise overlapping) Hamiltonians $\mathbf{H}_{[n]}$ from AGNR5 with a total length of 20 carbon rings. Each Hamiltonian $\mathbf{H}_{[n]}$ covers 2×2 carbon rings (28 atoms [20 C, 8 H] and 320 basis functions). n denotes the distance from the extracted subsystem to the border of the finite DFT system measured in carbon rings. (Calculation details: FHI-AIMS, basis set tier1, closed-shell, 284 atoms [200 C, 84 H], 3220 basis functions.)

between block Hamiltonians, we use two norms: the maximum norm $\|\Delta \mathbf{H}\|_{max}$ (referring to the maximal deviation in the corresponding matrix elements) and the Euclidean norm $\|\Delta \mathbf{H}\|_2$. As is seen in Figure 6, either norm rapidly converges to the bulk limit. In fact, we find that, e.g., $n = 9$ can be taken as a faithful approximation for the bulk block Hamiltonian, i.e., of one slice in the infinite 1D system ($n \to \infty$) and, therefore, we take it as our reference in Figure 6. We verified that the absolute convergence behavior for $\mathbf{V}$ is the same as that for $\mathbf{H}^{block}$ (data not shown).

3.3. Convergence Tests for the Transmission Coefficient. The matrix norms give an unbiased measure for the
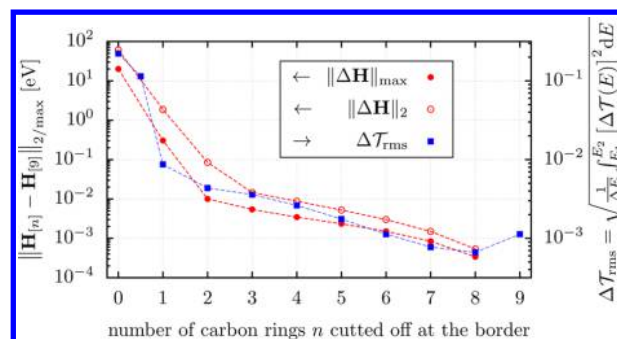
Figure 6. Dependence of the subsystem Hamiltonian $\mathbf{H}^{(n)}$ on its position in pristine AGNR5 with a length of 20 carbon rings. As matrix norms (left y-axis), we use the max norm $\|\Delta \mathbf{H}\|_{max} = max_{ij}(|\Delta \mathbf{H}_{ij}|)$ and the Euclidean norm $\|\Delta \mathbf{H}\|_2 = \sigma_{max}$, where σ_{max} is the largest singular value of $\Delta \mathbf{H}$. The root-mean-square deviation $\Delta \mathcal{T}_{rms}$ (right y-axis) is plotted to show differences in the transmission calculation; see Appendix B.1 for further details. The left and right arrows in the legend refer to the corresponding left and right y-axes.

convergence of the block Hamiltonian. In the physical context, however, one is more interested in the convergence of observables, which may or may not be well-represented by the unbiased measures that we have considered. Therefore, an independent check of the convergence of the transmission is indicated as well.

To this end, we performed a series of transport simulations using the set $\mathbf{H}^{block}_{[n]}$ to construct the corresponding sequence of self-energies. In Figure 6, we also display the root-mean-square of $\Delta \mathcal{T}(E)$, which is the deviation between the calculated transmission and its exact value. The latter is given by the number of bands of pristine AGNR5 at a certain energy (for bandstructure, cf. Figure 7 (left); for details on $\Delta \mathcal{T}_{rms}$, cf. Appendix B.1). To obtain a global measure, we have averaged $\Delta \mathcal{T}(E)$ over an energy interval $E_1 = \varepsilon_F - 3$ eV to $E_2 = \varepsilon_F + 3$ eV.
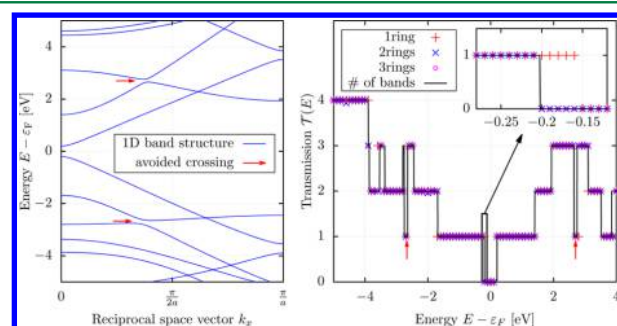
Figure 7. Left: Bandstructure of infinite one-dimensional pristine AGNR5 calculated with FHI-AIMS tier1. Right: Transmission function and number of bands for different sizes of $\mathbf{H}^{block}$ (using blocks with 1, 2, and 3 carbon rings in the transport direction). Note that the transmission calculation is even able to resolve the marked avoided crossings in the bandstructure. As required, the transmission functions drop by 2 in a low energy range at each avoided crossing.

At $n \geq 1$, the deviations in the transmission $\Delta \mathcal{T}_{rms}$ already drops below 10^{-2} and we see a regular convergence pattern. Hence, we conclude that very short extensions, actually only a single carbon ring wide, are sufficient to obtain quantitative transport coefficients in graphene ribbons.
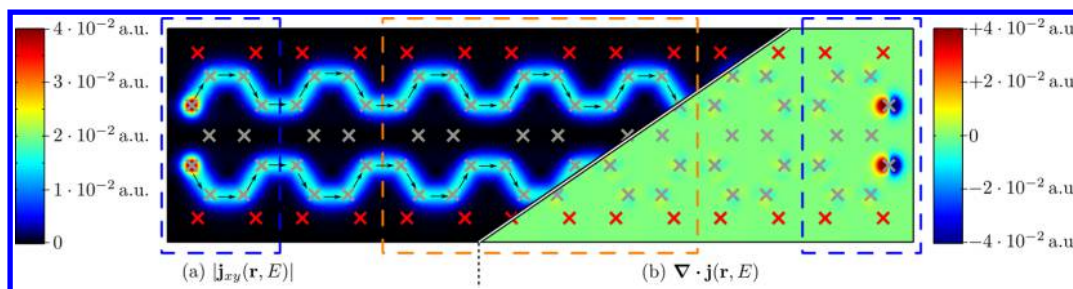
Figure 8. In-plane current density $\mathbf{j}_{xy}(\mathbf{r},E)$ (left) and current divergence $\nabla\cdot\mathbf{j}(\mathbf{r},E)$ (right) for pristine AGNR5 at $E = \varepsilon_F + 1$ eV, at a plane $z = 0.4$ Å above the carbon and hydrogen atoms (gray and red crosses, respectively). The current density carries one conductance quantum, $\mathcal{T}(E) = 1$; its direction is indicated by black arrows. The contact regions, where the self-energies representing the leads are added, are marked in blue dashed boxes. In these areas, artificial current sources and sinks are seen in the current density and in the divergence because the current appears from/disappears into the leads (cf. Appendix B.2. for further details). The orange dashed box is used for further convergence tests (see Figures 10 and 12). The arrows give the direction of the current density. (Calculation details: FHI-AIMS, basis set tier1, closed-shell.)

To further illustrate the validity of our method, we also display the energy-resolved convergence behavior in Figure 7 (right). Small deviations (up to 0.05 eV) are discernible only near steps (see inset in Figure 7). The exact positions of steps are recovered with minimally larger blocks (2 and 3 rings). We thus confirm our previous results.

Summarizing, we conclude that to achieve the numerical accuracy in the transport coefficients that we are after in this work it is sufficient for us to work with blocks $\mathbf{H}^{block}$ and $\mathbf{V}$ containing only one carbon ring; further coupling matrix elements can be neglected.

3.3.1. Remark on Damping Coefficients in $\hat{\eta}_{ABC}$. For the test calculations presented in Figures 6 and 7, the default parametrization for the leakage rate $\eta(\mathbf{r})$ (summarized after eq 21) has been used. We have ensured that our conclusions do not change under a moderate variation of the damping rate and its spatial arrangement (cf. Appendix B.1). Specifically, when the leakage rate is sufficiently large ($\eta_0 \approx 0.1{-}1$ Ha) and smoothly approaches zero near the device region ($\kappa L \approx 8{-}64$), the step-like transmission function is reproduced as long as the leads are long enough ($M \approx 50{-}200$). (This is consistent with our earlier work[41] for tight-binding models.)

We mention that the number of building blocks M needs to be adjusted manually because it depends on the width of the graphene ribbon. As a rule of thumb, the length of the total system should exceed its width at least by a factor of $L/W \approx 10{-}25$.[46]

4. LOCAL CURRENTS

So far, we have focused on global observables, like the transmission function $\mathcal{T}(E)$, that involve spatial averages (see eq 4). In this section, we discuss how to calculate spatially resolved observables, like the current density $\mathbf{j}(\mathbf{r})$.

4.1. Formalism. The current density can be represented as a spatial derivative of the Keldysh function

$$
\begin{aligned}
\mathbf{j}(\mathbf{r},E) &= \frac{1}{2\pi}\frac{\hbar}{2m}\lim_{\mathbf{r}'\to\mathbf{r}}(\nabla_{\mathbf{r}'}-\nabla_{\mathbf{r}})\,\mathbf{G}^{<}(\mathbf{r},\mathbf{r}',E)\\
&= \frac{1}{2\pi}\frac{\hbar}{2m}\lim_{\mathbf{r}'\to\mathbf{r}}(\nabla_{\mathbf{r}'}-\nabla_{\mathbf{r}})\sum_{ij}\tilde{\varphi}_i(\mathbf{r})\,\mathbf{G}^{<}_{ij}\tilde{\varphi}_j(\mathbf{r}')\\
&= \frac{1}{2\pi}\frac{\hbar}{m}\sum_{ij}\left[\tilde{\varphi}_i(\mathbf{r})\underbrace{\frac{1}{2}(\mathbf{G}^{<}_{ij}-\mathbf{G}^{<}_{ji})}_{=:\overset{as}{\mathbf{G}^{<}_{ij}}}(\nabla\tilde{\varphi}_j(\mathbf{r}))\right]\\
&= \frac{1}{2\pi}\frac{\hbar}{m}\sum_{ij}\tilde{\varphi}_i(\mathbf{r})\,\overset{as}{\mathbf{G}^{<}_{ij}}(\nabla\tilde{\varphi}_j(\mathbf{r}))
\end{aligned}
\tag{25}
$$

where $\overset{as}{\mathbf{G}^{<}}$ is an abbreviation for the antisymmetric elements of the lesser Green's function. Anticipating time reversal invariance of the KS system, the basis $|\tilde{\varphi}_i\rangle$ is chosen to be real so that all expansion coefficients $\tilde{c}_{ji}$ remain real as well.

Other local quantities, like the nonequilibrium density $n(\mathbf{r},E)$ or the local density of states $\rho(\mathbf{r},E)$, are calculated in a similar fashion.

4.1.1. Remarks on Discretization Errors Due to Finite Basis Set Sizes. The physical current density must fulfill the continuity equation $\nabla\cdot\mathbf{j}(\mathbf{r}) = 0$ at all points $\mathbf{r}$. The basis sets that we use (either numerical orbitals or Gaussian orbitals) are finite and thereby incomplete. Hence, the orthodox continuity equation is satisfied approximately and will be recovered only in the basis set limit. Therefore, in our calculations, we monitor the divergence

$$
\begin{aligned}
\nabla\cdot\mathbf{j}(\mathbf{r},E) &= \frac{1}{2\pi}\frac{\hbar}{m}\sum_{ij}\tilde{\varphi}_i(\mathbf{r})\,\overset{as}{\mathbf{G}^{<}_{ij}}(\Delta\tilde{\varphi}_j(\mathbf{r}))\\
&+ \frac{1}{2\pi}\frac{\hbar}{m}\underbrace{\sum_{ij}(\nabla\tilde{\varphi}_i(\mathbf{r}))\,\overset{as}{\mathbf{G}^{<}_{ij}}(\nabla\tilde{\varphi}_j(\mathbf{r}))}_{=0\ (\text{due to symmetry})}
\end{aligned}
\tag{26}
$$

and ensure that our observables are converged with respect to the size of the basis set.[47]

4.1.2. Finite Differences. The necessary derivatives of the basis functions $\varphi_i(\mathbf{r})$ are calculated numerically using a symmetric two-point rule ($\mathbf{e}_j$ are the canonical basis vectors)
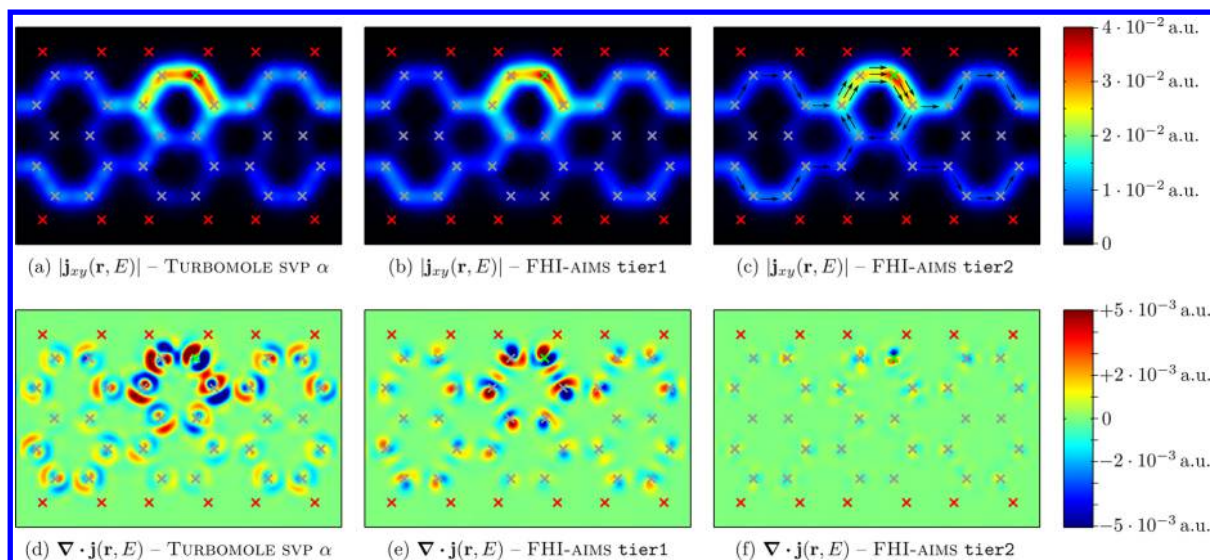
Figure 9. (a−c) Variation of the in-plane current density $j_{xy}(\mathbf{r},E)$ as the size of the basis set increases for AGNR5 with one nitrogen substituent (green cross) at a plane $z = 0.4$ Å above the carbon atoms restricted in the x-direction to the central region near the nitrogen impurity (orange dashed box in Figure 8). The current density carries half a conductance quantum, $\mathcal{T}(E) = 0.5$, in all cases; the energy E is varied such that all plots share the same transmission value; see the colored arrows in Figure 11 for the exact position. The current direction is indicated by black arrows for the largest basis set. (d−f) The divergence $\nabla \cdot \mathbf{j}(\mathbf{r},E)$ belonging to the respective current pattern in (a−c). The divergence converges very rapidly with the increasing size of the basis set. Divergence errors have a very minimal impact on the current pattern.

$$\nabla_j \varphi_i(\mathbf{r}) = (2\Delta)^{-1}[\varphi_i(\mathbf{r} + \Delta \mathbf{e}_j) - \varphi_i(\mathbf{r} - \Delta \mathbf{e}_j)],$$

$$\nabla_j^2 \varphi_i(\mathbf{r}) = \Delta^{-2}[\varphi_i(\mathbf{r} + \Delta \mathbf{e}_j) - 2\varphi_i(\mathbf{r}) + \varphi_i(\mathbf{r} - \Delta \mathbf{e}_j)] \tag{27}$$

We chose $\Delta = \sqrt[3]{\varepsilon}$ (with $\varepsilon = 2.2 \cdot 10^{-16}$ being double machine precision), leading to accuracies on the order of 10^{-10} and 10^{-5} for the first and second derivatives, respectively.[48]

4.2. Convergence Tests. As an application and test, we investigate the local electron current density in pristine and functionalized AGNR5. We raster the current and divergence formulas, eqs 25 and 26, on a Cartesian grid with a grid spacing of $\delta = 0.1$ Å.

4.2.1. Pristine AGNR5. In Figure 8, we show an electron current density map at $z = 0.4$ Å. (All atoms are located in the $z = 0$ plane.) A perfect streamline pattern arises as a consequence of quantum confinement in the transverse direction.[4] The plot illustrates the partitioning and how the current flow is generated in the NEGF approach. Within the left and right contact regions (blue boxes), the self-energy $\mathbf{\Sigma}_{L/R}$ is nonzero. Its anti-Hermitian piece generates the current flow, left source, and right drain. Outside the source and drain, the divergence of the current is seen to be very small and can be controlled by the size of the basis set.

4.2.2. AGNR5 with a Single Nitrogen Substituent. For the next application, one carbon atom near the border of AGNR5 is substituted by nitrogen (cf. Figure 2). The latter then acts as a strong scatterer. The atomistic equilibrium structure of the graphene lattice is hardly distorted and, in particular, is stable against out-of-plane perturbation. To ensure this stability, we tentatively placed the nitrogen atom 0.2 Å above the in-plane position of the substituted carbon atom. After geometry relaxation, the nitrogen returned into the planar position with an accuracy better than 10^{-4} Å.

We investigated the dependence of the current density on the basis set size (Figure 9). For a proper comparison, we need to account for a small shift of the KS-Hamiltonian due to the variation in the basis set size. Accordingly, we compared the current pattern based on the principle that we fix the transmission (rather than the energy) when going from a current pattern obtained for one basis set to the next one.

We observed a very rapid convergence of the current pattern. Only the divergence of the current exhibits a significant quantitative flow. As the basis set size increases (tier1 to tier2), the divergence decreases rapidly. Note that the basis sets SVP and tier1 are of equal size but differently constructed and, therefore, their divergence patterns also differ slightly.

An additional validation is to calculate the current density integrated over a cross-section at fixed x in the yz plane, $I_x = \iint j_x(\mathbf{r},E)\, \mathrm{d}y\, \mathrm{d}z$, and compare it with the total current (per energy and spin). The latter we have fixed by our choice to select the energy so that $\frac{e^2}{h}\mathcal{T}(E)$ is fixed. The ratio of both, $I_x/\mathcal{T}$, is reproduced in Figure 10 as a function of x. It deviates only slightly from unity, with an amplitude that reduces rapidly with increasing basis set size.

4.2.2.1. Remark on Magnetism. The nitrogen feeds an extra electron into the conduction band of the ribbon. Therefore, a question about spin-polarization and the Kondo effect arises.

Concerning the latter, we recall that the flat geometric structure suggests that the unpaired electron is not localized but completely immersed in the graphene π-band. Hence, we do not expect a Coulomb blockade-type situation. Our expectation is confirmed by an open-shell calculation that produces two (identical) half-occupied states at the Fermi energy, suggesting the absence of (nearby) magnetic instability. Hence, indications are that Kondo physics is not relevant in this system.

As one would expect after meeting these prerequisites, open- and closed-shell calculations yield the same transport behavior. For open-shell transport calculations, we still perform a closed-shell calculation of the lead system. Therefore, the self-energy representing the leads is spin-independent. The (spin collinear) open-shell Hamiltonian of the device region is block diagonal in the spin. Therefore, one can calculate all transport quantities by
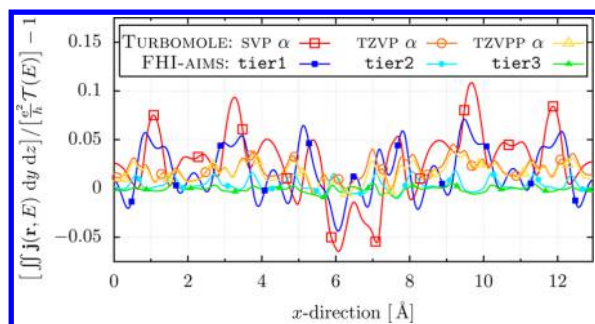
Figure 10. Relative deviation between the local current density integrated over a yz plane and the total current given by the transmission function. The x position of the integration plane is measured from the left side of the orange dashed box shown in Figure 8, coinciding with the plot range in Figure 9. Also, as in Figure 9, the transmission is fixed at $\mathcal{T} = 0.5$. For clarity, only the markers of every 12th sampling point are shown.
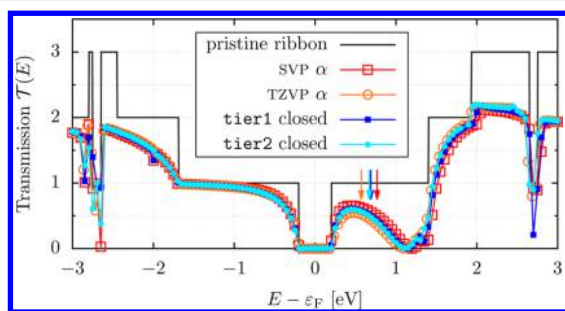
Figure 11. Dependence of the transmission function on basis set size and spin treatment (open- vs closed-shell calculation). The main differences are small shifts in energy. As an example, the energy points with $\mathcal{T}(E) = 0.5$ are marked with colored arrows. TURBOMOLE: only the α-channel of an open-shell calculation in the SVP and TZVP basis sets; FHI-AIMS: closed-shell calculation in the tier1 and tier2 basis sets.

using each spin block of the Hamiltonian separately. All transport quantities then carry a single spin index.

In Figure 11, we compare closed-shell calculations (with fractional occupation numbers using FHI-AIMS) with the major spin channel (α) of collinear open-shell calculations (with integer occupation numbers using TURBOMOLE). Indeed, we observed a good collapse of all data curves. For completeness, we note that the minor channel (β) looks slightly different due to different occupation numbers induced by an overall odd number of electrons in combination with the integer occupation number. When allowing for fractional occupation numbers as in FHI-AIMS, both spin channels feature the same transmission curve.

4.2.2.2. Convergence Tests for the Current Density. In Figure 12, we show the current pattern deviation (Δ_j), the current divergence ($\Delta_{\nabla\cdot j}$), and the comparison to transmission ($\Delta_{\mathcal{T}}$). All three are formulated as root-mean-square errors

$$\Delta_j = \sqrt{\frac{1}{V} \int d^3 r |\mathbf{j}(\mathbf{r},E) - \mathbf{j}_{\text{largestBasis}}(\mathbf{r},E)|^2} \tag{28}$$

$$\Delta_{\nabla\cdot j} = \sqrt{\frac{1}{V} \int d^3 r (\nabla\cdot\mathbf{j}(\mathbf{r},E))^2} \tag{29}$$

$$\Delta_{\mathcal{T}} = \sqrt{\int \frac{dx}{L_x}\left(I_x\Big/\left[\frac{e^2}{h}\mathcal{T}(E)\right] - 1\right)^2} \tag{30}$$
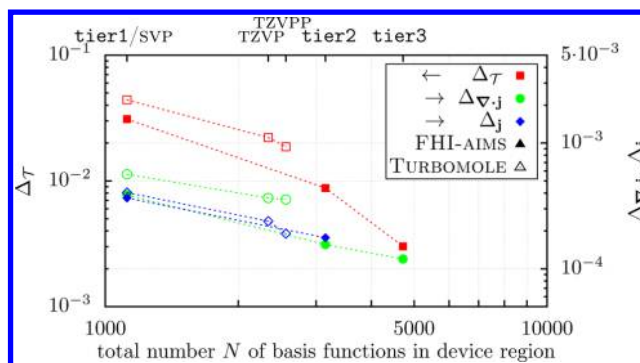
Figure 12. Convergence analyses of the local currents shown in Figure 9 with respect to the basis set using FHI-AIMS (closed markers) and TURBOMOLE (open markers). The root-mean-square deviations Δ_x are plotted over the number of basis functions per carbon atom ($\Delta_{\mathcal{T}}$ on left y-axis; Δ_j and $\Delta_{\nabla\cdot j}$ on right y-axis). All error measures decrease when increasing the basis set size. The different basis sets contain different numbers of basis functions per hydrogen/carbon/nitrogen atom: tier1/SVP: 5/14/14; TZVP: 6/31/31; TZVPP: 14/31/31; tier2: 15/39/39; tier3: 31/55/55. The left and right arrows in the legend refer to the corresponding left and right y-axes.

with $I_x = \iint j_x(\mathbf{r},E)\, dy\, dz$. In the case of the current pattern, an exact reference solution is not available, so we have to resort to the current pattern calculated with the largest basis set (tier3) for comparison. The spatial integrals are done by summing over the same grid points that were used to calculate the local currents, restricting the x-integration further to the (orange dashed box) central part of the device region (cf. Figure 8).[49]

All three error measures decrease when the basis set size increases, irrespective of the underlying DFT code. Interestingly, the error measures for the transmission ($\Delta_{\mathcal{T}}$) and for the divergence ($\Delta_{\nabla\cdot j}$) are, for the same basis set size, always smaller using FHI-AIMS basis sets compared to that using TURBOMOLE basis sets.

The results of this section are encouraging because they suggest that the local current density is an observable that rapidly converges with the size of the basis set. Thus, the smallest sets, SVP/tier1, already allow for quantitative results to be obtained.

4.3. Application: Effect of Lattice Relaxation on Transport. We now apply the presented method to larger systems and return to AGNR41, shown in Figure 1. We discussed the physical consequences of the current vortices seen there in a previous paper.[5] Here, we report important technical details, i.e., the convergence behavior with the basis set size. A new result will be related to the effect of the lattice relaxation on the transmission function.

4.3.1. Current Convergence. 4.3.1.1. Current Patterns. Figure 13 displays the current pattern of the large, mesoscopic sample for two different basis sets, tier1 and tier2. The visible deviations are located near the left/right boundaries with values at the lower end of the logarithmic colorscale (dark blue). In the upper 3 orders of magnitude, the current density is virtually identical.

4.3.1.2. Transmission Function. In Figure 14, the transmission functions corresponding to the current patters are also shown. At the energy chosen for Figure 13, $E = \varepsilon_F - 635$ meV (orange arrow), the transmission is well-converged, as expected. At other energies, slightly larger deviations can be seen that are mostly interpreted as small shifts of the resonance energies. Only in the relatively dense region of the spectrum do these
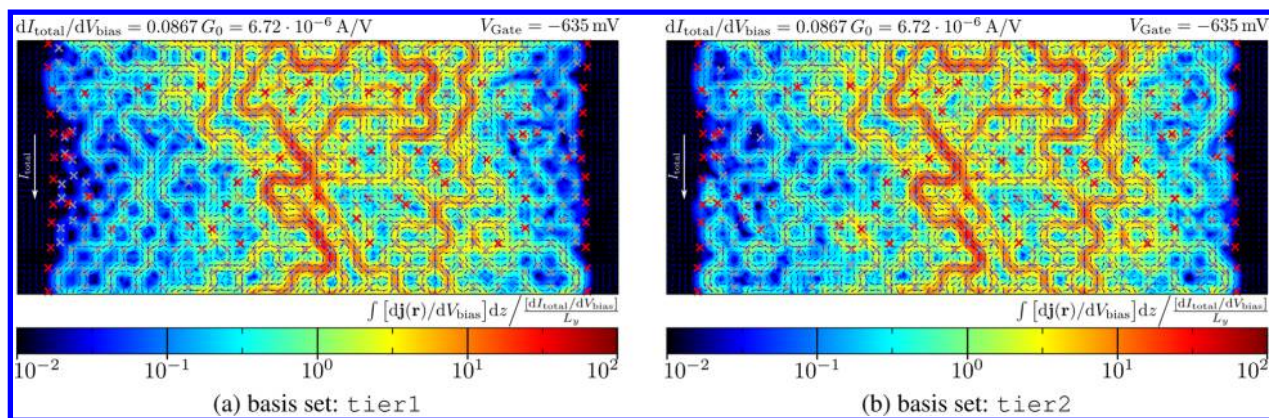
Figure 13. Basis set comparison of the local current density response (integrated over the out-of-plane direction) in AGNR41 of Figure 1 at energy $E = \varepsilon_F - 635$ meV (orange arrow in Figure 14). The current exhibits very strong mesoscopic fluctuations that exceed the average current by 2 orders of magnitude on the logarithmic color scale. The current density is plotted relative to average current density I/L_y, with width $L_y = 5.2$ nm. Plot shows current amplitude (color), current direction (arrows), carbon atoms (gray crosses), and hydrogen atoms (red crosses).
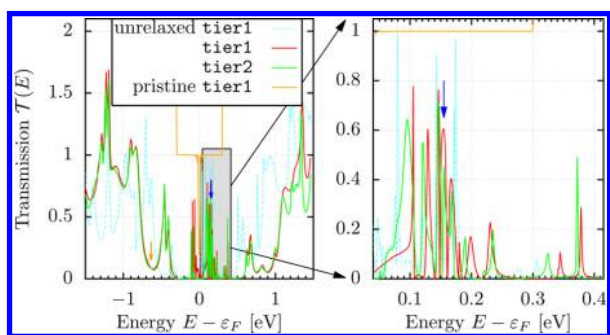
Figure 14. Transmission of AGNR41 shown in Figure 1 comparing the basis set convergence (tier1 vs tier2) of the relaxed structure with the deviation to the distorted (unrelaxed) structure with a tier1 basis set. Additionally, the number of channels of pristine AGNR41 is shown (orange).

shifts become comparable to the level spacing such that larger deviations occur. In these regions, differences in the current patterns can occur (see Appendix C for the current pattern at $E = \varepsilon_F + 155$ meV; blue arrow in Figure 14).

We conclude that a tier1 basis set already gives a qualitatively reliable transmission function, but for resolving the fine structure of the transmission, a larger basis set is required.

4.3.2. Lattice Relaxation. An important question arises that relates to the effect of lattice relaxation on the transport characteristics. To what extent is the transmission function sensitive to whether the atomistic geometry is fully relaxed into its equilibrium state? To address this question, we have obtained the transmission function (tier1) for an atomistic geometry that has not been relaxed.

Clearly, there is a certain arbitrariness in the selection of the unrelaxed reference state. For the qualitative information that we are after, here, it is sufficient to adopt the following procedure: We chose an unrelaxed structure consisting of a regular hexagonal carbon lattice with bond length $d_{CC} = 1.439$ Å. The hydrogen atoms terminating the ribbon have been placed as a continuation of the hexagonal lattice but with a bond distance of $d_{CH} = 1.0954$ Å. Both values are taken from the relaxation of a small 14 × 14 graphene ribbon calculation in TURBOMOLE using a SVP basis set. The adsorbed hydrogen atoms in the unrelaxed AGNR41 are then placed vertically above or below the carbon atom with a bond distance of d_{CH}. In the unrelaxed structure, the carbon atoms (with the adsorbed

hydrogen atoms) are moved out of the graphene plane by 0.5 Å to represent sp^3 hybridization. For the relaxed structure, we additionally structurally relax all atoms of the device region (excluding contact region) until all atomic forces drop below 10^{-2} eV/Å.

We show the change of the lattice constants due to relaxation in Table 1. The most important effect is that hydrogen

Table 1. Effect of Lattice Relaxation on the Bond Lengths d_{XY} (Measured between Atoms X and Y)[a]

	unrelaxed	relaxed
d_{HC_H}	1.095 Å	$1.119 \pm 0.008\binom{+0.017}{-0.013}$ Å
d_{HH}	1.439 Å	$2.100 \pm 0.024\binom{+0.031}{-0.039}$ Å
$d_{C_0C_0}$	1.439 Å	$1.428 \pm 0.024\binom{+0.055}{-0.072}$ Å
$d_{C_0C_H}$	1.523 Å	$1.513 \pm 0.010\binom{+0.024}{-0.030}$ Å
$d_{C_HC_H}$	1.439 Å	$1.566 \pm 0.016\binom{+0.028}{-0.014}$ Å

[a]To reduce boundary effects, we take only atoms into account that (a) were fully relaxed and (b) are at least three carbon atoms away from the ribbon boundary (in the y-direction). Atom types: hydrogen atom (H) adsorbed on a carbon atom (C_H) and carbon atoms (C_0) without any hydrogen adsorbates. In the case of two hydrogen atoms (d_{HH} or $d_{C_HC_H}$), both hydrogen atoms are located on the same side of the graphene flake. For relaxed AGNR41, the distances are given as $m \pm \sigma\binom{\Delta_{min}}{\Delta_{max}}$, where m is the average value, σ is the standard deviation, and $m + \Delta_{max/min}$ is the maximal/minimal value. In unrelaxed AGNR41, all distances are exact in the sense that no spatial variations exist.

adsorbates sitting on adjacent carbon atoms repel each other (d_{HH} grows) and also pull their anchor carbon atoms apart ($d_{C_HC_H}$ increases). This effect is also shown in Figure 15. Additionally, the bond lengths are no longer the same everywhere in the ribbon but depend on the local impurity configuration, e.g., the carbon–carbon bond length $d_{C_0C_0}$ (for carbon atoms without hydrogen adsorbates) deviates up to 5% from its average value.

The transmission function of the distorted lattice has also been displayed in Figure 14. Major modifications can be seen, especially at higher energies. Therefore, we conclude that the details of the transmission function, especially the peak positions, are sensitive not only to where the adsorbates are placed but also to their effect on the carbon lattice.
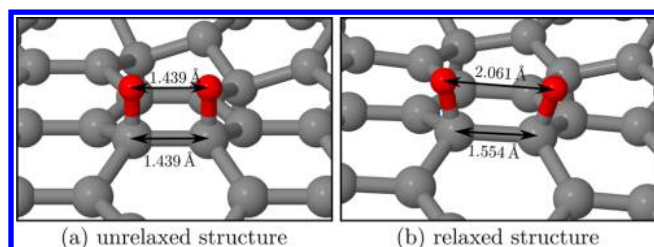
Figure 15. Example of lattice relaxation when two hydrogen adsorbates sit on neighboring carbon atoms. (a) Unrelaxed structure with hydrogen adsorbates placed directly above the carbon atoms (see text). (b) DFT-relaxed structure (see text). The hydrogen atoms (red spheres) repel each other to make room for their electron cloud. This also pushes the anchor carbon atoms (gray spheres) apart.
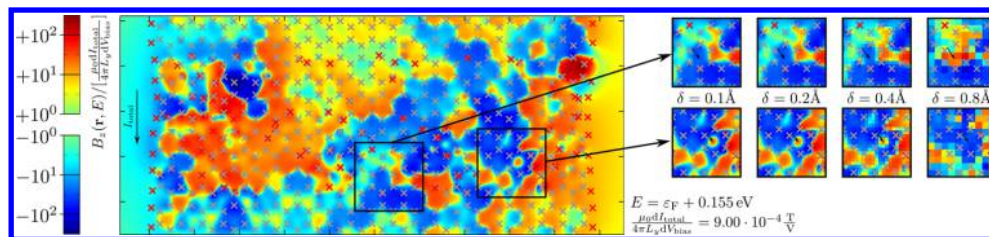
Our result might bear certain relevance for tight-binding simulations of disordered graphene flakes in the limit of large defect concentrations. Generic tight-binding studies ignore the crosstalk that two adsorbates can have via their interaction in terms of lattice strain. One would expect that this crosstalk plays an important role, at higher concentrations, for the optimal lattice geometry and, therefore, as our study shows, can feed back also into the electronic structure and the transmission function.

5. MAGNETIC FIELDS

The local current density is a physical observable that is not easy to measure in actual experiments. For that reason, it is important to consider indirect evidence of whether it exists. One obvious manifestation would be strong fluctuations in the local magnetic field that accompanies the current flow. Such magnetic fields could feed back into the current flow itself (self-induction). They could also potentially be detected in experimental setups that allow a measurement of the nuclear magnetic resonance (NMR) to be performed in the presence of the current flowing. For this reason, we believe that it is of interest to compute the field $\mathbf{B}(\mathbf{r})$ that accompanies the dc current flow.

5.1. Implementation of the Law of Biot−Savart. The integrals in eq 13 for the magnetic field $\mathbf{B}$ and magnetic moment $\mathbf{m}$ are readily evaluated on a properly chosen Cartesian grid with grid spacing δ, which was already used to raster the current density $\mathbf{j}(\mathbf{r})$ in the device region

$$\mathbf{m} = \frac{\delta^3}{2} \sum_{\mathbf{r}} (\mathbf{r} - \mathbf{O}) \times [-\mathbf{j}(\mathbf{r})]$$

(31)

$$\mathbf{B}(\mathbf{r}) = \alpha^2 \delta^3 \sum_{\substack{\mathbf{r}' \\ \mathbf{r}' \neq \mathbf{r}}} \frac{[-\mathbf{j}(\mathbf{r}')] \times (\mathbf{r} - \mathbf{r}')}{|\mathbf{r} - \mathbf{r}'|^3}$$

(32)

where, as usual, α denotes the fine structure constant. (The minus sign reflects the negative electron charge.) As usual, the definition of the dipole moment makes explicit reference to the origin of the coordinate system, $\mathbf{O}$. In order to eliminate spurious contributions to $\mathbf{m}$ originating from the leads, we chose the center of the integration box for $\mathbf{O}$. The sum over $\mathbf{r}'$ explicitly omits the singular point $\mathbf{r} = \mathbf{r}'$; it does not contribute because the angle integration of the vector quantity over the surface of the associated volume element vanishes.

5.2. Convergence Tests: Grid Spacing Dependence. As with any discretization, the magnetic field $\mathbf{B}(\mathbf{r})$ and magnetic moment $\mathbf{m}$ carry a residual dependence on the grid spacing δ that vanishes in the continuum limit $\delta \to 0$.

5.2.1. Magnetic Field Pattern. In Figure 16, the grid dependence of the spatial magnetic field pattern is displayed: $\mathbf{B}(\mathbf{r}, E = \varepsilon_F + 0.155 \text{ eV})$; cf. blue arrow in Figure 14. At grid spacings $\delta \lesssim 0.2$ Å, the magnetic pattern is converged.

5.2.2. Global Deviations. In order to obtain more quantitative information, we also consider the discretization error for quantities that average over the entire sample.

The magnetic moment, which is associated with the magnetic field shown in Figure 16, is $\mathbf{m}_{\delta=0}(E) = (0.03, -0.01, -1.51)$ μ_B/V (extrapolated for $\delta \to 0$). In Figure 17, we show the
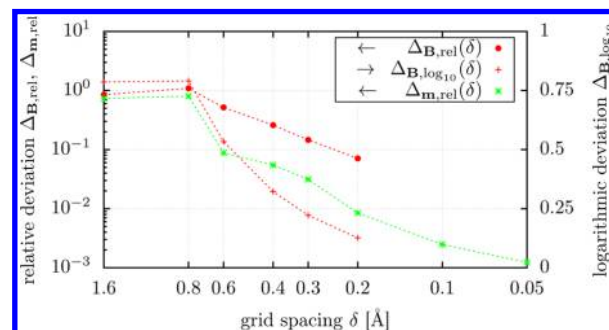
Figure 17. Relative mean root square and logarithmic deviations of the magnetic field $\mathbf{B}(\mathbf{r}, E = \varepsilon_F + 0.155 \text{ eV})$ and the magnetic moment $\mathbf{m}(E = \varepsilon_F + 0.155 \text{ eV})$ depending on the grid spacing δ. The grid spacing is used for both rastering the current and integrating over space. The left and right arrows in the legend refer to the corresponding left and right y-axes.

relative root-mean-square deviation of the magnetic moment and how it converges when taking the continuum limit.

Figure 16. Convergence of the magnetic field distribution (in the out-of-plane direction) induced by the current distribution at energy $E = \varepsilon_F + 155$ meV (blue arrow in Figure 14; cf. Appendix C, Figure 23). The magnetic field strongly varies and changes sign from region to region. On the right side, the convergence of the magnetic field with respect to the grid spacing δ is shown. Note that some features (marked by a black arrow) simply vanish when employing too coarse of a grid, e.g., $\delta = 0.8$Å.

$$\Delta_{(\mathbf{m}),\mathrm{rel}}(\delta) = \frac{\sqrt{|\mathbf{m}_\delta(E) - \mathbf{m}_{\delta=0}(E)|^2}}{\sqrt{|\mathbf{m}_{\delta=0}(E)|^2}} \tag{33}$$

As is seen there, the magnetization rapidly converges, reaching accuracies better than 1% at $\delta \lesssim 0.2$ Å.

Data for a similar convergence test for the magnetic field $\mathbf{B}(\mathbf{r})$ with

$$\Delta_{\mathbf{B},\mathrm{rel}}(\delta) = \frac{\sqrt{\frac{1}{V}\int_\delta \mathrm{d}^3\mathbf{r}|\mathbf{B}_\delta(\mathbf{r},E) - \mathbf{B}^{\mathrm{finestGrid}}(\mathbf{r},E)|^2}}{\sqrt{\frac{1}{V}\int_\delta \mathrm{d}^3\mathbf{r}|\mathbf{B}^{\mathrm{finestGrid}}(\mathbf{r},E)|^2}} \tag{34}$$

are also displayed in Figure 17. In order to reduce the numerical effort, here the reference point is taken to be the calculation with the finest computational feasible grid, which is $\delta^{\mathrm{finestGrid}} = 0.1$ Å for $\mathbf{B}(\mathbf{r})$. The symbol $\int_\delta$ indicates a summation over the grid with spacing δ. At $\delta \lesssim 0.2$ Å, the relative discretization error drops below 10%, which we feel is acceptable given that the raw data is spread over 4 orders of magnitude.

In order to better account for the logarithmically broad distribution in magnetic field strengths, we introduce a logarithmic measure for the discretization error

$$\Delta_{\mathbf{B},\log_{10}}(\delta)$$
$$= \sqrt{\frac{1}{V}\int_\delta \mathrm{d}^3\mathbf{r}\sum_{i=1}^3 \|\log_{10}[\mathbf{B}_i(\mathbf{r},E)/\mathbf{B}_i^{\mathrm{finestGrid}}(\mathbf{r},E)]\|^2} \tag{35}$$

effectively a root-mean-square error for the exponents. Again, there is a clear convergence behavior; see Figure 17. At $\delta \lesssim 0.3$ Å, the logarithmic deviation already falls below a quarter decade, so deviations are hardly visible in logarithmic plots like Figure 16.

6. PERFORMANCE

In our DFT calculation of larger systems exceeding 1000 carbon atoms, we rely on FHI-AIMS. It uses the ELPA[34] package tuned for petaflop applications to solve the Kohn−Sham eigenvalue problem on massive parallel computer clusters. The scalability of FHI-AIMS has been shown previously.[30] Therefore, we restrict ourselves to discussing the performances of the transport modules; the KS states of the DFT reference calculation and the eigenvector representation of the corresponding overlap matrix S are assumed to be given and stored on the hard disk (HDF5 file[50]).

The observables that we consider for benchmarking are the transmission $\mathcal{T}$ and the current density $\mathbf{j}(\mathbf{r})$; our test systems are hydrogen-saturated AGNRs of four different sizes (Figure 18). Further parameters are as follows: tier1 basis set (14 basis functions per C and 5 per H), self-energy iterated $M = 200$ times, and resolution of the real space grid of $\delta = 0.2$ Å, with 31 lattice points in the z-direction. The performance validations were carried out at the High Performance Computing Center Stuttgart (HLRS) on the CRAY XE6 (Hermit) cluster. Each node is equipped with $2\cdot16 = 32$ cores (Dual Socket AMD Interlagos @2.3 GHz 16 cores) with 1 to 2 GiB RAM per core.

6.1. Scaling of Computational Time and Memory.
Figure 19 displays how the memory ($\mathcal{M}$) and CPU time (T) requirements scale with the system size parametrized by the number of basis functions, N. As is seen from the fits, the memory requirement scales with N^2 (number of elements in
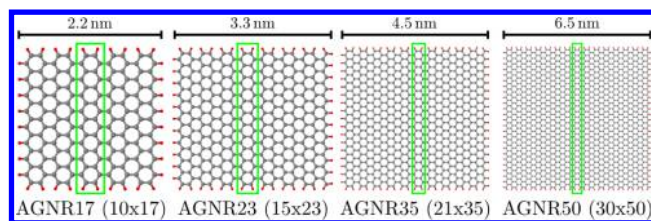
Figure 18. AGNRs used for benchmarking from left to right: 170 carbon atoms (10×17), 345 (15×23), 735 (21×35), and 1500 (30×50). The size of the block $\mathbf{H}^{\mathrm{block}}$ used to build the lead is marked in green (one carbon ring in the transport direction); the whole system (including hydrogen termination) is used as the device $\mathbf{H}^{\mathrm{device}}$.
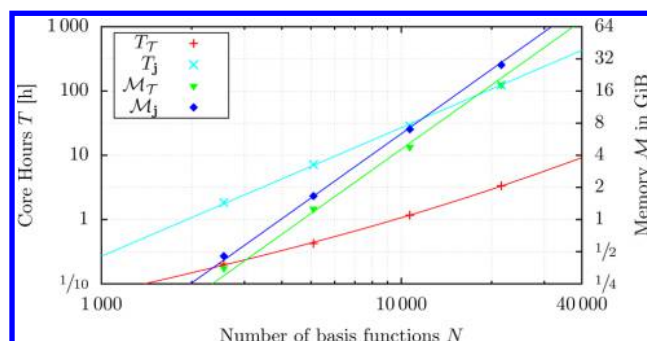
Figure 19. Left axis: Core hours (wall time times number of CPU cores) $T_\mathcal{T}$ and $T_\mathbf{j}$ for calculating transmission $\mathcal{T}$ and current density $\mathbf{j}$ per energy point (average value for 128 energy points). Right axis: The corresponding memory requirements $\mathcal{M}_\mathcal{T}$ and $\mathcal{M}_\mathbf{j}$. The solid lines are the following fits (with $n = N/10\,000$): $T_\mathcal{T} = (0.660n + 0.409n^2)$ h, $T_\mathbf{j} = 26.8n^2$ h, $\mathcal{M}_\mathcal{T} = 4.55n^2$ GiB, and $\mathcal{M}_\mathbf{j} = 6.37n^2$ GiB.

the Green's functions). The computational time for the current calculation also scales like a second-order polynomial in N (and not third order) because the overlap of basis functions at different atoms is negligible beyond a distance that exceeds the several bond lengths.

6.2. Parallelizability.
The data presented in Figure 19 has been obtained with a single MPI process ($N_{\mathrm{MPI}} = 1$) parallelized using threads on $p = 32$ CPU cores. We now report on the speedup that we achieve using MPI to run several processes (each combining $p = 8$ CPU cores) on different computational nodes. Then, the wall time (total real-world calculation time) $T_{N_{\mathrm{MPI}}}$ decreases with the number of processes N_{MPI}; ideally, it is inversely proportional to it.

In Figure 20, we plot the reduction factor (inverse speedup) $S^{-1} = T_{N_{\mathrm{MPI}}}/T_1$ over the inverse number of MPI processes, N_{MPI}^{-1}. According to Amdahl's law, $S^{-1} = [\alpha + (1 - \alpha)/N_{\mathrm{MPI}}]$, the serial fraction of the code, i.e., the saturation α, can be estimated via the y-intercept of the corresponding fits ($S^{-1}|_{N_{\mathrm{MPI}}^{-1}=0} = \alpha$; see inset in Figure 20). This turns out to be $\alpha \approx 1\%$ for 10 675 basis functions. In other words, the present parallelization will cease to be efficient at $\alpha N_{\mathrm{MPI}} \approx 1$, i.e., at $\sim$1000 cores.

7. CONCLUSIONS AND SUMMARY

A formalism has been presented to calculate the (charge) current density $\mathbf{j}(\mathbf{r})$ and the induced orbital fields $\mathbf{B}(\mathbf{r})$. It is based on the nonequilibrium Green's function (NEGF) technique and density functional theory (DFT) formulated in atom-centered basis sets.
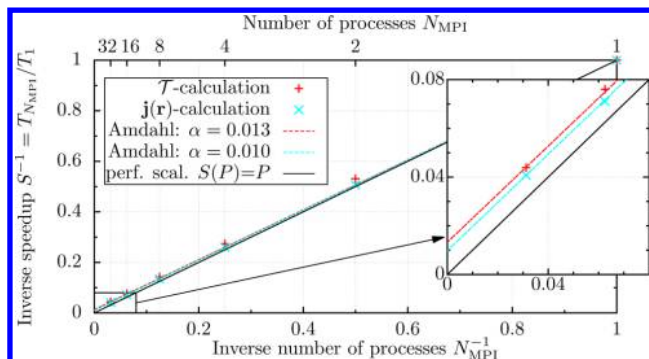
Figure 20. Scaling behavior when using N_{MPI} processes, each using $p = 8$ cores, which communicate via MPI with each other. For AGNR35 (21 × 35) containing $N = 10\,675$ basis functions, $n_E = 128$ transmission values and $n_E = 32$ current densities have been calculated, ensuring that every process can calculate on a separate energy point. This benchmark employs up to 256 CPU cores.

The presented implementation is especially geared toward quasi-one-dimensional wires. Then, the leads can be dealt with by employing a standard recursive Greens-function method (decimation technique). Due to an extensive test of the computational parameters, we establish the reproducibility of our results. In particular, we ascertain that despite the numerical discretizations the continuity equation is fulfilled.

For the important application to the case of graphene ribbons, our results suggest that a moderate basis set (14 basis function per carbon atom; double-ζ quality) is already sufficient for simulating quantitatively correct current patterns. Larger basis sets are needed if small energy shifts in the transmission function are unacceptable.

Finally, we have employed the computational tool described here in order to test the impact of lattice relaxations on the transmission function $\mathcal{T}(E)$ of chemically functionalized graphene. We observe two transmission functions that hardly correlate with respect to the peak positions if the relaxed lattice is replace by an unrelaxed one that establishes local sp^3 geometry in an approximate *ad hoc* implementation only.

A. IMPLEMENTATION DETAILS

A.1. A Word on the Employed Löwdin Orthogonalization

Technically, the underlying DFT codes work with non-orthogonal atom-centered basis sets $|\varphi_i\rangle$. Internally, the Kohn−Sham (KS) orbitals $|\psi_i^{mo}\rangle$ are represented by expansion coefficients c_{ji} with respect to the non-orthogonal basis set, i.e., $|\psi_i^{mo}\rangle = \sum_j |\varphi_j\rangle c_{ji}$.

We use the (symmetric) overlap matrix $S_{ij} = \langle \varphi_i | \varphi_j \rangle$ to calculate the orthogonal set of basis functions $|\tilde{\varphi}_i\rangle$ via the Löwdin-orthogonalization[51] procedure, i.e., $|\tilde{\varphi}_i\rangle = \sum_j |\varphi_j\rangle [S^{-1/2}]_{ji}$. The square root $S^{1/2}$ is defined by the positive square roots of the eigenvalues in eigenbasis representation. The expansion coefficients are transformed as well: $\tilde{c}_{ik} = \sum_j [S^{1/2}]_{ij} c_{jk}$.

The Löwdin-orthonormalized basis set $|\tilde{\varphi}_i\rangle$ is the orthogonal basis set that minimizes the squared distance $\sum_i \int |\varphi_i(\mathbf{r}) - \tilde{\varphi}_i(\mathbf{r})|^2 \, d^3\mathbf{r}$ to the original basis set $|\varphi_i\rangle$.[52] In particular, this means that the orthonormalized basis function $|\tilde{\varphi}_i\rangle$ is still localized around the same atom core as $|\varphi_i\rangle$.

The full reconstructed KS Hamiltonian $\hat{\mathcal{H}}_0^{KS}$

$$\hat{\mathcal{H}}_0^{KS} = \sum_n |\psi_n^{mo}\rangle \varepsilon_n^{mo} \langle \psi_n^{mo}| = \sum_{ij} |\tilde{\varphi}_i\rangle \mathbf{H}_{0,ij}^{KS} \langle \tilde{\varphi}_j| \tag{36}$$

is readily written with respect to the orthonormal basis as

$$\mathbf{H}_{0,ij}^{KS} = \sum_n \tilde{c}_{in} \varepsilon_n^{mo} [\tilde{c}^T]_{nj} \tag{37}$$

In the main part of the article, we always worked with the Löwdin-orthonormalized basis set $|\tilde{\varphi}_i\rangle$, even when calculating local observables [cf. eqs 25 and 26].

In practice, it is computationally advantageous to transform Green's functions to a non-orthogonal basis set, e.g., $\check{\mathbf{G}} = S^{-1/2} \mathbf{G} S^{-1/2}$, and calculate the local observables using the original non-orthogonal basis set. For the calculation of the current density, this means

$$\mathbf{j}(\mathbf{r},E) = \frac{1}{2\pi} \frac{\hbar}{m} \sum_{ij} \tilde{\varphi}_i(\mathbf{r}) \overset{\text{as}}{\mathbf{G}_{ij}^<} (\nabla \tilde{\varphi}_j(\mathbf{r})),$$

$$= \frac{1}{2\pi} \frac{\hbar}{m} \sum_{\substack{ii' \\ jj'}} \varphi_i(\mathbf{r}) \underbrace{S_{i'i}^{-1/2} \overset{\text{as}}{\mathbf{G}_{ij}^<}(E) \, S_{jj'}^{-1/2}}_{=:\check{\mathbf{G}}_{i'j'}^<} (\nabla \varphi_{j'}(\mathbf{r})) \tag{38}$$

Going to the second line, we replaced the orthonormal basis set $\tilde{\varphi}_i(\mathbf{r})$ with the original set $\varphi_i(\mathbf{r})$ using the overlap matrix S.

A.2. Optimization: Exploiting the Block Structure of Self-Energy Σ and Broadening Matrix Γ

Formally, transmission $\mathcal{T}$ and Keldysh Green's function $\mathbf{G}^<$ are calculated as described in the main text of the article

$$\mathcal{T}(E) = \text{Tr}\{\mathbf{\Gamma}_L \mathbf{G} \mathbf{\Gamma}_R \mathbf{G}^\dagger\} \tag{39}$$

cf. eq 4

$$\mathbf{G}^<(E) = i\mathbf{G}\mathbf{\Gamma}_L \mathbf{G}^\dagger \tag{40}$$

cf. eq 8.

In practice, the matrices $\mathbf{\Gamma}_{L/R} = i(\mathbf{\Sigma}_{L/R} - \mathbf{\Sigma}_{L/R}^\dagger)$ contain a lot of zeros. Their non-vanishing entries belong to the left/right contact areas of the device region. This block structure is evident if one partitions the device region into three regions: left contact area (L), right contact area (R), and the remaining central part of the device (C). In the basis (L/C/R), the matrices $\mathbf{\Gamma}_{L/R}$ then read

$$\mathbf{\Gamma}_L = \begin{pmatrix} \tilde{\mathbf{\Gamma}}_L & 0 & 0 \\ 0 & 0 & 0 \\ 0 & 0 & 0 \end{pmatrix}, \qquad \mathbf{\Gamma}_R = \begin{pmatrix} 0 & 0 & 0 \\ 0 & 0 & 0 \\ 0 & 0 & \tilde{\mathbf{\Gamma}}_R \end{pmatrix} \tag{41}$$

Working with the (unnecessarily large) matrices $\mathbf{\Gamma}_{L/R}$ is computationally inefficient. It is much more efficient to also partition the retarded Green's function $\mathbf{G}$ into blocks, i.e.

$$\mathbf{G} = \begin{pmatrix} \mathbf{G}_{LL} & \mathbf{G}_{LC} & \mathbf{G}_{LR} \\ \mathbf{G}_{CL} & \mathbf{G}_{CC} & \mathbf{G}_{CR} \\ \mathbf{G}_{RL} & \mathbf{G}_{RC} & \mathbf{G}_{RR} \end{pmatrix}, \qquad \mathbf{G}_{FL} := \begin{pmatrix} \mathbf{G}_{LL} \\ \mathbf{G}_{CL} \\ \mathbf{G}_{RL} \end{pmatrix} \tag{42}$$

Here, we already defined $\mathbf{G}_{FL}$ as the submatrix of $\mathbf{G}$ where the first index refers to the full (F) device region but the second index is restricted to the left (L) contact region.

Using these shrunken matrices, the transmission $\mathcal{T}$ and Keldysh Green's function $\mathbf{G}^<$ are calculated as

$$\mathcal{T}(E) = \text{Tr}\{\tilde{\boldsymbol{\Gamma}}_{\text{L}} \mathbf{G}_{\text{LR}} \tilde{\boldsymbol{\Gamma}}_{\text{R}} [\mathbf{G}_{\text{LR}}]^{\dagger}\} \qquad (43)$$

$$\mathbf{G}^{<}(E) = i\mathbf{G}_{\text{FL}} \tilde{\boldsymbol{\Gamma}}_{\text{L}} [\mathbf{G}_{\text{FL}}]^{\dagger} \qquad (44)$$

A.3. Remark on Complexity

Using this technique, the computational complexity for calculating the transmission and Keldysh Green's function is reduced from $O(N^3)$ [eqs 39 and 40] to $O(n^3)$ [eq 43] and $O(nN^2)$ [eq 44]. N and n denote the number of basis functions in the device region and the left contact region, respectively.

B. MODELING THE LEADS

We present additional convergence validations for parameters used in the self-energies representing the leads. First, in Appendix B.1, we discuss the influence of different damping rate parametrizations on the transmission through pristine AGNR5. We find that a wide range of physically reasonable parameters lead to a correct transmission function. Second, in Appendix B.2, we discuss the spatial effect of the self-energy on the current flow in the contact regions of the central device. We realize that the self-energy effectively behaves as current source and sink.

B.1. Convergence Tests for the Transmission Coefficient

To test the damping model (see Section 2.2) and the extraction procedure (e.g., in Figure 6), we compare the transmission as calculated with different parametrizations of the damping rate $\eta(\mathbf{r})$ with the (numerically) exact result (derived from a bandstructure calculation). Our test systems are pristine armchair nanoribbons with five transverse carbon atoms (AGNR5). To this end, we define the root-mean-square deviation $\Delta\mathcal{T}_{\text{rms}}$

$$\Delta\mathcal{T}_{\text{rms}} = \sqrt{\frac{1}{\Delta E} \int_{E_1}^{E_2} [\Delta\mathcal{T}(E)]^2 \, dE} \qquad (45)$$

$$\Delta E = E_2 - E_1 \quad E_{1/2} = \varepsilon_{\text{F}} \mp 3 \text{ eV} \qquad (46)$$

The integral is evaluated on an energy grid with spacing $\Delta = 0.1\text{eV}$; $\Delta\mathcal{T}(E)$ denotes the difference of the calculated transmission and the number of bands in the bandstructure in the interval $(E - \Delta, E + \Delta)$, formally

$$\Delta\mathcal{T}(E) = \min_{\tilde{E}\in(E-\Delta, E+\Delta)} |\mathcal{T}_{\text{calc}}(E) - N_{\text{bands}}(\tilde{E})| \qquad (47)$$

where $N_{\text{bands}}(\tilde{E})$ is the number of bands at energy $\tilde{E}$. Table 2 list the deviations of the transmission functions for different parametrizations of the damping rate $\eta(\mathbf{r})$ (see eq 21).

We have therefore verified that when the leakage rate is sufficiently large ($\eta_0 \approx 0.1$–1 Ha) and is smoothly reduced to zero near the device region ($\kappa L \approx 8$–64) then exact results (in this case, a step-like transmission function) can be recovered as long as the leads are long enough ($M \approx 50$–200). As a rule of thumb, the length of the total system should exceed its width at least by a factor of $L/W \approx 10$–25.

If these conditions are mistreated, then more drastic effects arise, such as standing waves reflecting from the lead boundaries. For illustration, Figure 21 focuses on these effects induced by poorly chosen damping models. Finite values of η at the device-to-lead interface cause back-reflection of waves. The latter happens for step-function parametrization as well as for too large damping at the interface ($\kappa L \leq 4$).

Table 2. Variation of the Calculated Transmission Coefficients (Measured with Respect to Conducting Bands, cf. Figure 7) with Different Parametrizations of the Damping Rate $\eta(\mathbf{r})$, see eq 21[a]

number of unit cells	
M	$\Delta\mathcal{T}_{\text{rms}}$
1	$3.7 \cdot 10^{-1}$
5	$1.2 \cdot 10^{-1}$
10	$2.7 \cdot 10^{-2}$
50	$6.9 \cdot 10^{-3}$
100	$8.3 \cdot 10^{-3}$
200	**$6.6 \cdot 10^{-4}$**

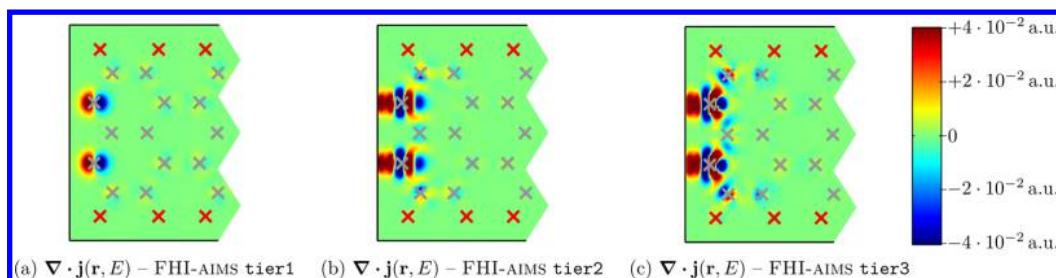| damping model		
model		$\Delta\mathcal{T}_{\text{rms}}$
$\eta_0 = 0.1\,\text{Ha}$		$6.6 \cdot 10^{-3}$
$\eta_0 = 0.5\,\text{Ha}$	$\kappa L = 16$	$2.3 \cdot 10^{-3}$
$\eta_0 = 1.0\,\text{Ha}$		**$6.6 \cdot 10^{-4}$**
	$\kappa L = 4$	$2.6 \cdot 10^{-1}$
	$\kappa L = 8$	$2.6 \cdot 10^{-3}$
$\eta_0 = 1.0\,\text{Ha}$	**$\kappa L = 16$**	**$6.6 \cdot 10^{-4}$**
	$\kappa L = 32$	$7.8 \cdot 10^{-3}$
	$\kappa L = 64$	$1.8 \cdot 10^{-3}$
$\eta_{\text{step},0} = 0.1\,\text{Ha}$	$\eta_{\text{step}}(x)$	$5.4 \cdot 10^{-1}$
$\eta_{\text{step},0} = 1.0\,\text{Ha}$		$6.6 \cdot 10^{-1}$

[a]The default values taken in our production runs are listed in underlined bold type. Entries leading to acceptable results are marked in green, and unacceptable ones are marked in red. Top: Variation with the number of blocks M used in each lead. Bottom: Variation with damping rate $\eta(\mathbf{r})$. Different values for the parameters η_0 (top) and κ (center) of the damping rate from eq 21 are tested, as well as a step-function parametrization $\eta_{\text{step}}(d) = \eta_{\text{step},0} \cdot \Theta(d)$ (bottom).
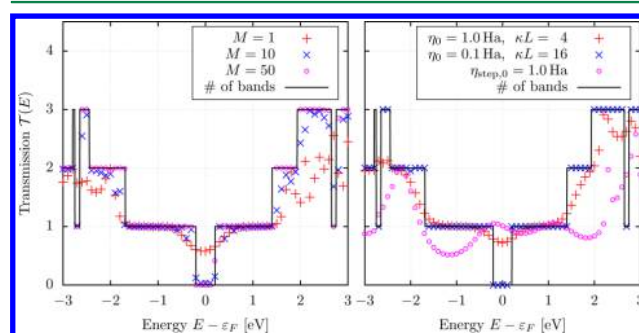

Figure 21. Transmission $\mathcal{T}$ of pristine AGNR5 for several damping models, including nonconverged ones for illustration. The exact value, the number of bands from a bandstructure calculation, is plotted as a solid line. Left: The length of the leads (number of building blocks M) is varied (the remaining parameters are the default values: $\eta_0 = 1$ Ha, $\kappa L = 16$). For too short leads ($M \leq 10$), the steps in the transmission function are not yet fully developed. Right: The length of the leads is fixed ($M = 200$), but the parametrization of the leakage rate $\eta(\mathbf{r}_i)$ is varied, i.e., to a step function (constant at $\eta_{\text{step},0}$ in the leads but zero in the device region; magenta circle markers), which shows standing wave patterns due to reflection at the interface.

B.2. Artificial Current Sources and Sinks in the Contact Region

When coupling to the leads, the current density artificially appears and disappears, as seen in Figure 22 in terms of the divergence pattern $\nabla \cdot \mathbf{j}(\mathbf{r}, E)$ in the left contact region. The self-energy Σ_{L} effectively behaves as a current source with a spatial structure that becomes more complicated for large basis sets. Therefore, the calculated current density represents the physical current density only in regions away from the contact region, i.e., in the center of the device region, but it does not in the model electrodes. The effect of the self-energy can even

(a) $\nabla \cdot \mathbf{j}(\mathbf{r}, E)$ – FHI-AIMS tier1 (b) $\nabla \cdot \mathbf{j}(\mathbf{r}, E)$ – FHI-AIMS tier2 (c) $\nabla \cdot \mathbf{j}(\mathbf{r}, E)$ – FHI-AIMS tier3

Figure 22. Current divergence $\nabla \cdot \mathbf{j}(\mathbf{r}, E)$ in the left contact region (coupled to the left lead) for pristine AGNR5 at a plane $z = 0.4$ Å above the carbon atoms. The self-energy $\mathbf{\Sigma}_L$ effectively behaves as a current source with a spatial structure that becomes more complicated for large basis sets. Note the different scale, which is larger by about 1 order of magnitude than all the other divergence plots in this article.

(a) basis set: tier1 (b) basis set: tier2
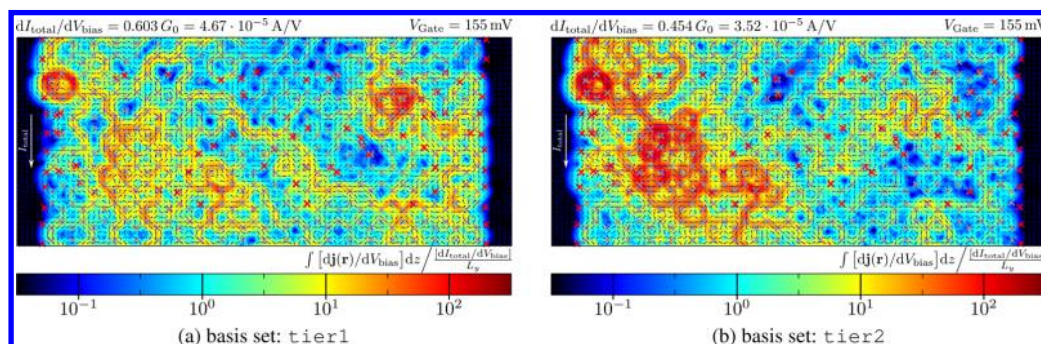
Figure 23. Basis set comparison of the local current density response (integrated over the out-of-plane direction) in the AGNR41 of Figure 1 at energy $E = \varepsilon_F + 155$ meV (blue arrow in Figure 14). The current density is plotted relative to average current density I/L_y, with width $L_y = 5.2$nm. Plot shows current amplitude (color), current direction (arrows), carbon atoms (gray crosses), and hydrogen atoms (red crosses).

spread a little further into the device region since the basis functions have a finite extension. Thus, in our convergence tests, we compared only the current density in a smaller region (orange dashed box in Figure 8), which is one additional carbon ring away from the contact region.

C. BASIS SET CONVERGENCE FOR THE CURRENT FLOW IN AGNR41 WITH 20% HYDROGEN ADSORBATES

Figure 23 shows the basis set dependence of the current density at an energy point where the transmission itself if not yet fully converged but where small energy shifts are noticeable in the transmission peaks (cf. blue arrow in Figure 14). In this situation, the current density still exhibits a dependence on the size of the basis set. The main qualitative feature remains: current vortices are still present and stable. Also, quantitative features are sustained; the overall scale is the same, and the current still exhibits mesoscopic fluctuations on the same order of magnitude, exceeding the average current by 2 orders of magnitude (cf. the logarithmic color scale). Hence, we are unable to predict the concrete current path at a certain energy point when using a small tier1 basis set. Normally, this is not a real issue since one would not trust the exact current pattern anyway due to the absence of a formal justification of KS transport in this general system. Nevertheless, we can still make meaningful predictions about the statistical properties of the current densities (such as the magnitude of the fluctuations or their mean value) even though the transmission function is not yet converged with respect to the size of the basis set.

AUTHOR INFORMATION

Corresponding Author

*E-mail: michael.walz@kit.edu.

REFERENCES

(1) Castro Neto, A. H.; Guinea, F.; Peres, N. M. R.; Novoselov, K. S.; Geim, A. K. *Rev. Mod. Phys.* **2009**, *81*, 109−162.

(2) Peres, N. M. R. *Rev. Mod. Phys.* **2010**, *82*, 2673−2700.

(3) Das Sarma, S.; Adam, S.; Hwang, E. H.; Rossi, E. *Rev. Mod. Phys.* **2011**, *83*, 407−470.

(4) Wilhelm, J.; Walz, M.; Evers, F. *Phys. Rev. B: Condens. Matter Mater. Phys.* **2014**, *89*, 195406.

(5) Walz, M.; Wilhelm, J.; Evers, F. *Phys. Rev. Lett.* **2014**, *113*, 136602.

(6) Pecchia, A.; Penazzi, G.; Salvucci, L.; Di Carlo, A. *New J. Phys.* **2008**, *10*, 065022.

(7) Brandbyge, M.; Mozos, J.-L.; Ordejón, P.; Taylor, J.; Stokbro, K. *Phys. Rev. B: Condens. Matter Mater. Phys.* **2002**, *65*, 165401.

(8) Rocha, A.; García-Suárez, V.; Bailey, S.; Lambert, C.; Ferrer, J.; Sanvito, S. *Phys. Rev. B: Condens. Matter Mater. Phys.* **2006**, *73*, 085414.

(9) Rungger, I.; Sanvito, S. *Phys. Rev. B: Condens. Matter Mater. Phys.* **2008**, *78*, 035407.

(10) Calzolari, A.; Marzari, N.; Souza, I.; Buongiorno Nardelli, M. *Phys. Rev. B: Condens. Matter Mater. Phys.* **2004**, *69*, 035108.

(11) Brandbyge, M.; Mozos, J.-L.; Ordejón, P.; Taylor, J.; Stokbro, K. *Phys. Rev. B: Condens. Matter Mater. Phys.* **2002**, *65*, 165401.

(12) Taylor, J.; Guo, H.; Wang, J. *Phys. Rev. B: Condens. Matter Mater. Phys.* **2001**, *63*, 245407.

(13) Evers, F.; Weigend, F.; Koentopp, M. *Phys. Rev. B: Condens. Matter Mater. Phys.* **2004**, *69*, 235411.

(14) Aradi, B.; Hourahine, B.; Frauenheim, T. *J. Phys. Chem. A* **2007**, *111*, 5678−5684.

(15) Soler, J. M.; Artacho, E.; Gale, J. D.; García, A.; Junquera, J.; Ordejón, P.; Sánchez-Portal, D. *J. Phys.: Condens. Matter* **2002**, *14*, 2745.

(16) Giannozzi, P.; et al. *J. Phys.: Condens. Matter* **2009**, *21*, 395502.

(17) Cresti, A.; Van Tuan, D.; Soriano, D.; Cummings, A. W.; Roche, S. *Phys. Rev. Lett.* **2014**, *113*, 246603.

(18) Mabillard, J.; Can, T.; Morr, D. K. *New J. Phys.* **2014**, *16*, 013054.

(19) Kumar, S. B.; Jalil, M. B. A.; Tan, S. G.; Liang, G. *J. Phys.: Condens. Matter* **2010**, *22*, 375303.

(20) Zârbo, L. P.; Nikolić, B. K. *Europhys. Lett.* **2007**, *80*, 47001.

(21) Tuovinen, R.; Perfetto, E.; Stefanucci, G.; van Leeuwen, R. *Phys. Rev. B: Condens. Matter Mater. Phys.* **2014**, *89*, 085131.

(22) Rickhaus, P.; Makk, P.; Liu, M.-H.; Tóvári, E.; Weiss, M.; Maurand, R.; Richter, K.; Schönenberger, C. *Nat. Commun.* **2015**, *6*, 6470.

(23) Groth, C. W.; Wimmer, M.; Akhmerov, A. R.; Waintal, X. *New J. Phys.* **2014**, *16*, 063065.

(24) Wimmer, M.; Adagideli, I.; Berber, S.; Tománek, D.; Richter, K. *Phys. Rev. Lett.* **2008**, *100*, 177207.

(25) Liu, M.-H.; Richter, K. *Phys. Rev. B: Condens. Matter Mater. Phys.* **2012**, *86*, 115455.

(26) The problem of lacking spatial information is already apparent in the simplest examples. Consider a infinitely long circular wire carrying a spatially homogeneous current I_0. The wire radius R is the unknown spatial information. According to Ampère's circuital law, the azimuthal magnetic field inside the wire (at distance r to the wire center) is $B_\varphi = \frac{\mu_0 I_0}{2\pi} \frac{r}{R^2}$ and therefore strongly depends on the (unknown) wire radius R. For infinitesimal thin wires, the magnetic field diverges. This dependence becomes even more pronounced when dropping the homogeneity assumption of the current density.

(27) Bagrets, A. *J. Chem. Theory Comput.* **2013**, *9*, 2801−2815.

(28) Arnold, A.; Weigend, F.; Evers, F. *J. Chem. Phys.* **2007**, *126*, 174101.

(29) Wilhelm, J.; Walz, M.; Stendel, M.; Bagrets, A.; Evers, F. *Phys. Chem. Chem. Phys.* **2013**, *15*, 6684−6690.

(30) Blum, V.; Gehrke, R.; Hanke, F.; Havu, P.; Havu, V.; Ren, X.; Reuter, K.; Scheffler, M. *Comput. Phys. Commun.* **2009**, *180*, 2175−2196.

(31) Ahlrichs, R.; Bär, M.; Häser, M.; Horn, H.; Kölmel, C. *Chem. Phys. Lett.* **1989**, *162*, 165−169.

(32) Havu, V.; Blum, V.; Havu, P.; Scheffler, M. *J. Comput. Phys.* **2009**, *228*, 8367−8379.

(33) Auckenthaler, T.; Blum, V.; Bungartz, H. J.; Huckle, T.; Johanni, R.; Krämer, L.; Lang, B.; Lederer, H.; Willems, P. R. *Parallel Comput.* **2011**, *37*, 783−794.

(34) Marek, A.; Blum, V.; Johanni, R.; Havu, V.; Lang, B.; Auckenthaler, T.; Heinecke, A.; Bungartz, H.-J.; Lederer, H. *J. Phys.: Condens. Matter* **2014**, *26*, 213201.

(35) Wilhelm, J.; Walz, M.; Evers, F. *Phys. Rev. B: Condens. Matter Mater. Phys.* **2015**, *92*, 014405.

(36) Tröster, P.; Schmitteckert, P.; Evers, F. *Phys. Rev. B: Condens. Matter Mater. Phys.* **2012**, *85*, 115409.

(37) Stefanucci, G.; Kurth, S. *Phys. Rev. Lett.* **2011**, *107*, 216401.

(38) Bergfield, J. P.; Liu, Z.-F.; Burke, K.; Stafford, C. A. *Phys. Rev. Lett.* **2012**, *108*, 066801.

(39) Evers, F.; Schmitteckert, P. *EPL* **2013**, *103*, 47012.

(40) Evers, F.; Schmitteckert, P. *Phys. Status Solidi B* **2013**, *250*, 2330−2341.

(41) Evers, F.; Arnold, A. In *CFN Lectures on Functional Nanostructures: Nanoelectronics*; Röthig, C., Schön, G., Vojta, M., Eds.; Springer: Berlin, 2011; Vol. 2, Chapter 2.

(42) Foà Torres, L. E. F.; Roche, S.; Charlier, J.-C. *Introduction to Graphene-Based Nanomaterials: From Electronic Structure to Quantum Transport*; Cambridge University Press: New York, 2014.

(43) Ren, X.; Rinke, P.; Blum, V.; Wieferink, J.; Tkatchenko, A.; Sanfilippo, A.; Reuter, K.; Scheffler, M. *New J. Phys.* **2012**, *14*, 053020.

(44) Calculations presented throughout the article were carried out using the generalized gradient approximation (PBE exchange-correlation functional). In the case of TURBOMOLE, we have employed contracted Gaussian-type basis sets[53,54] of double-ζ (split-valence, DEF2-SVP) and triple-ζ quality with polarization functions (DEF2-TZVP, DEF2-TZVPP) and corresponding Coulomb-fitting basis sets within the resolution of identity approximation. These basis sets are abbreviated SVP, TZVP, TZVPP in this article. In the case of FHI-AIMS, sets of numerically tabulated atomic orbitals[30] have been employed with increasing precision, ranging from tier1 (double-ζ) through tier2 (triple-ζ) up to tier3 (quadruple-ζ) quality. For both codes, the basis functions $\varphi_i(\mathbf{r}) = \langle \mathbf{r} | \varphi_i \rangle$ are represented in a radial-angular decomposition, $\varphi_i(\mathbf{r}) = R_i(r) \, Y_{lm}(\theta, \phi)$ with real-values spherical harmonics Y_{lm} that ensure real-valued basis functions everywhere; the angular indices $l(i)$, $m(i)$ are functions of the overall basis index i. FHI-AIMS: numeric atom-centered orbitals (NAO),[30] the radial part $u_i(r) = R_i(r) \cdot r$ is numerically tabulated on a logarithmic grid. We employ a cubic spline interpolation for intermediate values. TURBOMOLE: contracted Gaussian type orbitals (CGTO),[53] whose radial part is given by $R_i(r) = r^l \sum_p^{P_i} d_p \exp(-\eta_p r^2)$, where P_i Gaussians with exponents η_p are contracted using the weights d_p.

(45) Since we are examining transport in armchair ribbons, the left and right borders of the finite system are of zigzag type. These zigzag borders facilitate spin separation, especially for ribbons that are not much longer than they are wide.[55] These spin separations do not describe the infinitely extended system, which we intend to investigate. Therefore, we suppress the spin separation using spin-unpolarized DFT simulations. The remaining finite-size effects (caused by the difference between hydrogen termination and carbon continuation in the x-direction) are dealt with by choosing large enough extensions $\mathbf{H}^{\text{ext}}$.

(46) For AGNR5, containing two carbon rings in width, the rule of thumb means that values $M = 2 \cdot L/W \approx 20-50$ are reasonable. For wider ribbons, larger values are needed, i.e., for AGNR41, containing 20 carbon rings in width, values of $M = 20 \cdot L/W \approx 200-450$ are necessary for converged leads. Compare this with Figure 14 (left), where the bandgap, calculated with $M = 200$, of pristine AGNR41 is not yet fully developed. The (theoretical sharp) step near $E = \varepsilon_F$ is still slightly smoothed.

(47) The continuity equation reflects particle number conservation. Since the KS-Hamiltonian is Hermitian also in the truncated (finite size) Hilbert space, there is an analogue of the continuity equation for each basis set size that eventually flows into the conventional one, $\nabla \cdot \mathbf{j}(\mathbf{r}) = 0$ in the basis set limit. In principle, one can speed up the convergence by working with this analogue continuity equation and the corresponding expressions for the current density in the reduced subspace. However, we can easily reach converged results without this trick, and for this reason, we here do not need it.

(48) The functional error of the symmetric two-point rule for the first and second derivatives with spacing Δ scales with $O(\Delta^2)$. Therefore, a small Δ should be chosen. On the other hand, calculating differences is numerically unfavorable because of a finite machine precision ε (double precision: $\varepsilon = 2.2 \cdot 10^{-16}$). The finite precision error scales with $O(\varepsilon \Delta^{-1})$ and $O(\varepsilon \Delta^{-2})$ for first and second derivative calculations, respectively. Since we need only the second derivative for the divergence, which is not a physical quantity but a convergence

measure, we sacrifice its accuracy in favor of a uniform Δ and choose an optimal $\Delta = \sqrt[3]{\varepsilon}$ for the first derivative, leading to accuracies on the order of 10^{-10} and 10^{-5} for the first and second derivatives, respectively. The units used in the code are atomic units, i.e., Bohr radius for the length scale, which is the correct length scale on which the basis function varies.

(49) The absolute value of the error measures Δ_j and $\Delta_{\nabla \cdot j}$ depend (arbitrarily) on the upper and lower integration borders in the y and z directions. Away from AGNR5, the local currents and the divergence are exactly zero, giving no measurable error. Because of the averaging procedure, the error measures Δ_j and $\Delta_{\nabla \cdot j}$ can become arbitrarily small by integrating over sufficient space. To compare the error measures, it is important to always perform the integration on the same grid.

(50) The HDF Group, Hierarchical Data Format, version 5. http://www.hdfgroup.org/HDF5/.

(51) Löwdin, P.-O. *J. Chem. Phys.* **1950**, *18*, 365−375.

(52) Carlson, B. C.; Keller, J. M. *Phys. Rev.* **1957**, *105*, 102−103.

(53) Schäfer, A.; Horn, H.; Ahlrichs, R. *J. Chem. Phys.* **1992**, *97*, 2571−2577.

(54) Weigend, F.; Ahlrichs, R. *Phys. Chem. Chem. Phys.* **2005**, *7*, 3297−3305.

(55) Fujita, M.; Wakabayashi, K.; Nakada, K.; Kusakabe, K. *J. Phys. Soc. Jpn.* **1996**, *65*, 1920−1923.